Supporting Information

Unlocking the Local Structure of Hard Carbon to Grasp Sodium-ion Diffusion Behavior for Advanced Sodium-ion Battery

Xin Feng[a, b], Yu Li[a, b*], Ying Li[a], Mingquan Liu[a, b], Lumin Zheng[a], Yuteng Gong[a], Ripeng Zhang[a], Feng Wu[a, b], Chuan Wu[a, b*], Ying Bai[a, b*]

X. Feng, Dr. Y. Li, Y. Li, M. Liu, L. Zheng, Y. Gong, R. Zhang, Prof. F. Wu, X. Prof. C. Wu, Prof. Y. Bai
School of Materials Science and Engineering
Beijing Institute of Technology
Beijing 100081, P.R. China
E-mail: liyu0820@bit.edu.cn; chuanwu@bit.edu.cn; membrane@bit.edu.cn

X. Feng, Y. Li, M. Liu, Prof. F. Wu, Prof. C. Wu, Prof. Y. Bai
Yangtze Delta Region Academy of Beijing Institute of Technology
Jiaxing 314019, PR China

Experimental Section

Preparation of hard carbons based on 1-methylimidazole (MMZ), pyridine (py), isoquinoline (IQL), aniline (BA), 2-methyl-5-nitroimidazole (MNMZ).

In a simple hydrothermal reaction process, 1-methylimidazole, pyridine, isoquinoline, aniline, 2-methyl-5-nitroimidazole (purchased from Aladdin industrial biochemical Co., Ltd., and used as received without further purification) and hexachlorobutadiene (purchased from Shanghai Chemical Reagent station-packing plant and used as receives, HCBD) were added into 50 mL steel autoclave coated with Teflon and sonicated for one hour to mix well, which molar ratios are both 3:1. Subsequently, the steal autoclave reactor was then placed in an oven for 6h at 200 °C After the reactor was cooled down to room temperature (25 °C) naturally, black solid product was collected and stored in a desiccator, and polymer precursors of different nitrogen-containing organic molecules are synthesized. Then the sample was put into a square corundum boat and annealed at 1200 °C for 2 h at a ramping rate of 5 °C min^{-1}, and the sample was maintained at that temperature for 2 h under Ar atmosphere. After cooling down to room temperature under Ar atmosphere, hard carbon materials were synthesized based on polymer precursors of different nitrogen-containing organic molecules (Labeled as MMZ, py, IQL, BA, and MNMZ, respectively). The related HC uniforms were all obtained by annealing at 1200 °C under argon protection, termed MMZ, py, IQL, BA, and MNMZ, respectively.

1.2 Characterizations

Scanning electron microscopy (SEM) images were obtained using a field emission Nova Nanosem 200 system operated at an acceleration voltage of 15 kV. Both transmission electron microscopy (TEM) and high-resolution transmission electron microscopy (HRTEM) were performed on JEM-2100F instrument. Energy dispersive spectroscopy (EDS) measurements

were also carried out using TEM (JEM-2100F). The composition and chemical states of the synthesis of polymer precursors were evaluated Fourier transform infrared (FTIR, Nicolet, NEXUS 670). X-ray photoelectron spectroscopy (XPS) was performed on a spectrometer from PHI QUANTERA-II SXM, using Mono Al Kα (1486.71eV) radiation at a power of 120 W (8 mA, 15 kV). X-ray diffraction (XRD) was conducted on a Smartlab SE Advance diffractometer using Cu Kα radiation (λ =0.15406 nm), with which the data was collected in the 2θ range of 10–80° at scan rate of 0.05°/min. Nitrogen adsorption-desorption isotherms at 77 K was measured on a Micromeritics Tristar 3000 system using vacuum-degassed samples (300 °C for 6 h). The isotherms were used to calculate the specific surface area and pore size distribution by the Brunauer-Emmett-Teller (BET) method. Raman spectra were performed on HR550 instrument using light source wavelength 532 nm, grating 18000. Thermogravimetric analysis (TGA, STA 449F5, NETZSCH) and TG-MS (Netzsch, QMS403C) was applied to understand the mass loss behavior and the volatile small molecular substances during carbonization with a heating rate of 10 °C/min under N_2 atmosphere.

1.3 Electrochemical measurements

To fabricate the electrode, active materials (MMZ, py, IQL, BA, and MNMZ), PVDF (dissolved in nitrogen methyl pyrrolidone, NMP) and super P were mixed in a mortar at a mass ratio of active materials: PVDF: super P of 8: 1: 1 to form the slurry, which was subsequently coated onto Cu foil and dried at 120°C for 12 h in a vacuum oven. NIBs were assembled using 2025 button batteries, with the electrode as the anode, sodium as the counter electrode (reference electrode), glass fiber (Whatman, GF/C, USA) as the separator, and 1 M $NaPF_6$ dissolved in EC/EDC (volume ratio, 1:1) as electrolyte. The loading mass of the HC for the tests is 0.8~1.2 mg cm^{-2}. The assembly of the button battery is completed in a glove box filled with argon. The galvanostatic charge and discharge (GCD) test is performed on the battery tester (Wuhan, LANHE, CT2001A). Cyclic voltammetry (CV) and electrochemical

impedance spectroscopy (EIS) measurements are carried out on electrochemical workstation (CHI-660E).

1.4 Related calculation formulas[1-3]

$$L(nm) = \frac{k\lambda}{\beta \cos \theta} \qquad \textbf{(S1)}$$

$$N = \frac{L_c}{d} \qquad \textbf{(S2)}$$

Where L is the thickness or length of graphite crystallites, β is the full width at half-maximum of the XRD peak, and λ is the wavelength of the X-rays used (0.154 nm). With K values of 1.84 and 0.90 for the (100) and (002) peaks of the carbon materials, respectively. n is the number of graphitic layer, d is the interlayer spacing.

$$D = \frac{4}{\pi \tau} \left(\frac{m_B V_m}{M_{BS}} \right)^2 \left(\frac{\Delta E_s}{\Delta E_t} \right)^2 \qquad \textbf{(S3)}$$

where m_B is the mass of the active material, V_m is the molar volume of the material, MB is the molar mass of carbon, S is the contact surface area of the electrode, τ is the pulse duration (600 s), ΔE_s is the steady state voltage change, and ΔE_t is the voltage change during current pulse application.

$$i = av^b \qquad \textbf{(S4)}$$

in which b=1 and 0.5 indicate a capacitance- and diffusion-controlled process of electrode.

$$\ln I(q) = \ln I(0) - \frac{1}{3} R_G^2 q^2 \qquad \textbf{(S5, Guinier)}$$

Where $I(q)$ is the scattering intensity at different scattering vectors. $I(0)$ is the scattering intensity at q=0, q=4πsinθ/λ is the scattering vector, and R_G is the gyration radius[4].

1.5 Density functional theory calculation section

All density functional theory (DFT) calculations within the generalized gradient approximation (GGA) using the Perdew-Burke-Ernzerhof (PBE) formulation were carried out using the Vienna Ab Initio Package (VASP)[5-7]. We use a plane wave basis set with a kinetic

energy cutoff of 500 eV to describe the ionic cores and incorporate valence electrons using projected augmented wave (PAW) potentials[8,9]. Using the Gaussian smearing technique and a width of 0.2 eV, partial occupancies of the Kohn–Sham orbitals were permitted. When the energy change was less than 105 eV, the electronic energy was regarded as self-consistent. For this calculation, the Brillouin zone was combined with a Monkhorst-Pack 1×2×1 k-point grid. When the energy change was less than 0.02 eV Å^{-1}, a geometry optimization was deemed to have reached convergence. By using empirical correction and the DFT+D3 method in Grimme's scheme, the weak interaction was described[10, 11].

The NGN-Na interaction, denoted as E_b(NGN-Na), is defined here as the binding energy of a single metal atom adsorbed on the graphene nanosheet as follows:

$$E_b(NGN\text{-}Na)=E_{NGN\text{-}Na}-E_{NGN}-E_{Na} \quad (S6)$$

where $E_{NGN\text{-}Na}$, E_{NGN}, and E_{Na} are the energies of the N doped graphene nanosheet with an isolated metal atom, pristine graphene (with or without N-doped), and an isolated metal atom, respectively. The Na-Na interaction, denoted as E_b(Na-Na), is defined as the binding energy of two isolated metal atoms in vacuum reference state for studying quasi-metallic clusters as follows:

$$E_b \text{ (Na-Na)}= E_{2Na} - 2E_{Na} \quad (S7)$$

where E_{2Na} is the energy of a metal dimer in the vacuum. It is worth noting that the Na-Na interaction defined here is different from the cohesive energy of bulk metal, which was defined and used for studying metal plating.[12,13] Similar to the previous reports,[14] the chemical potential (μ) of Na insertion on the carbon layers is specially defined for quantitatively describing the NGN-Na and Na–Na interactions as follows:
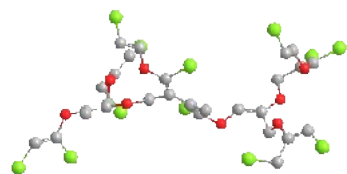
$$\mu = \frac{E_{NGN-Na}-E_{NGN}-n \times E_{Na}}{n} \quad (S8)$$

5

where $E_{NGN-nNa}$ is the energy of the graphene with metal atoms (n corresponds to the number of metal atoms).[15] While n=1, μ equals to $E_b(NGN-Na)$. While n > 1, μ is determined by both $E_b(NGN-Na)$ and $E_b(Na-Na)$.
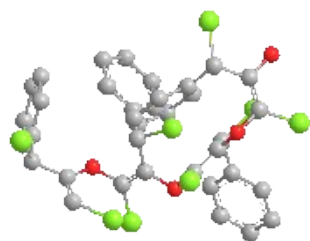
2. Supporting Figures and Table
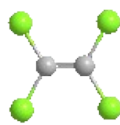
(Tetrachloroethylene does not react with this type of nitrogen-containing organic molecule)[16]

(The reaction of non-fully halogenated olefins with this class of nitrogen-containing organic molecules is not easy to control the spatial configuration)

(The reaction of aromatic hydrocarbons with this class of nitrogen-containing organic molecules, where the spatial configuration is not a planar configuration, is not suitable for this reaction)
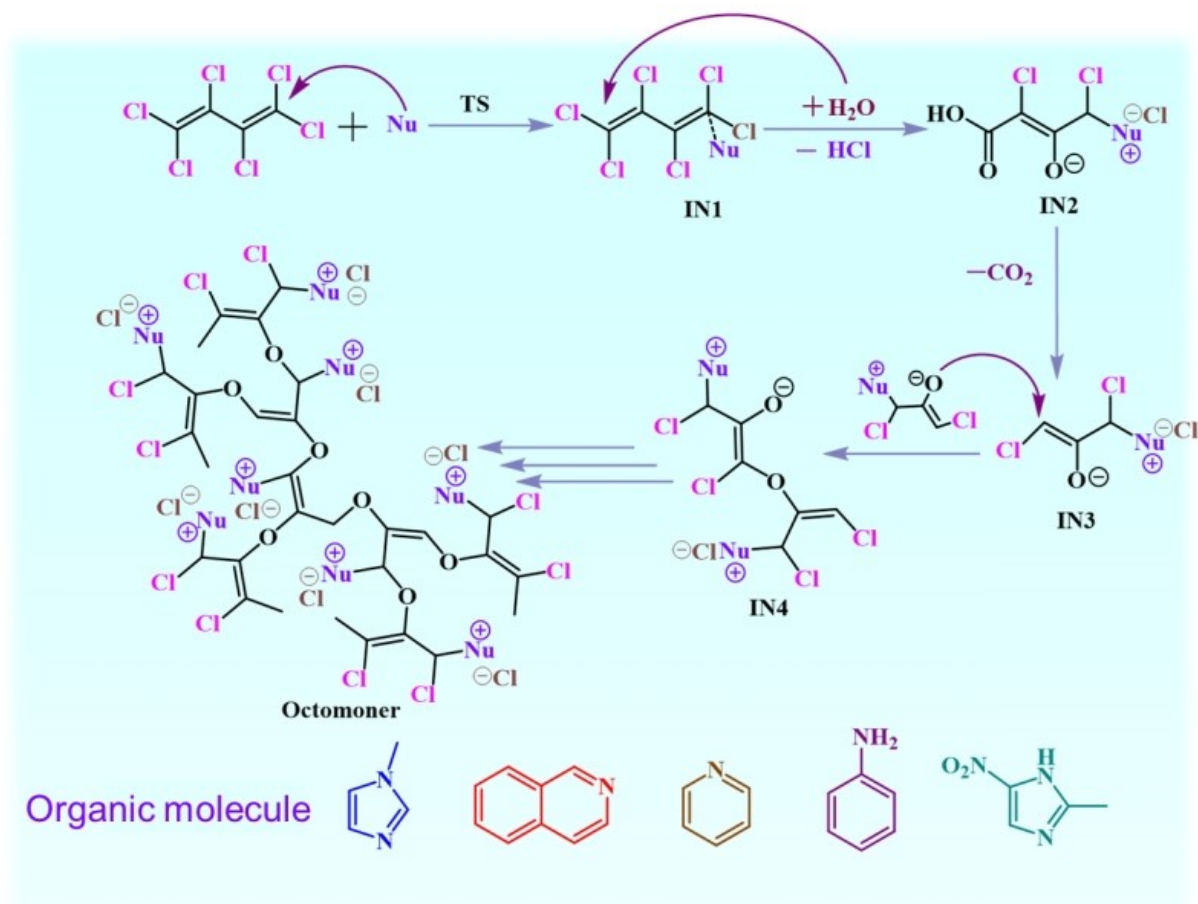
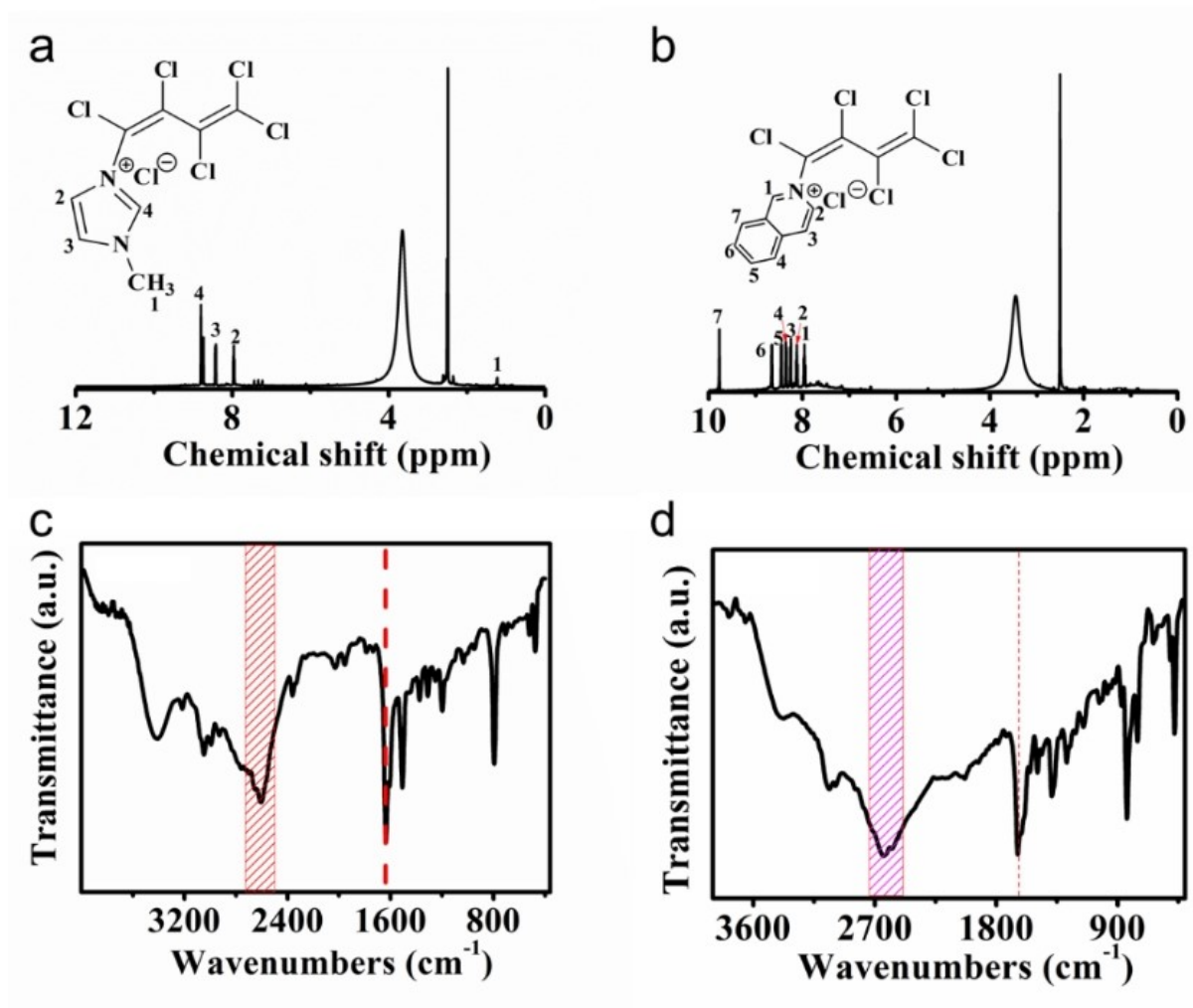**Scheme 1** Details for the substitutions, decarboxylation and octomoner.

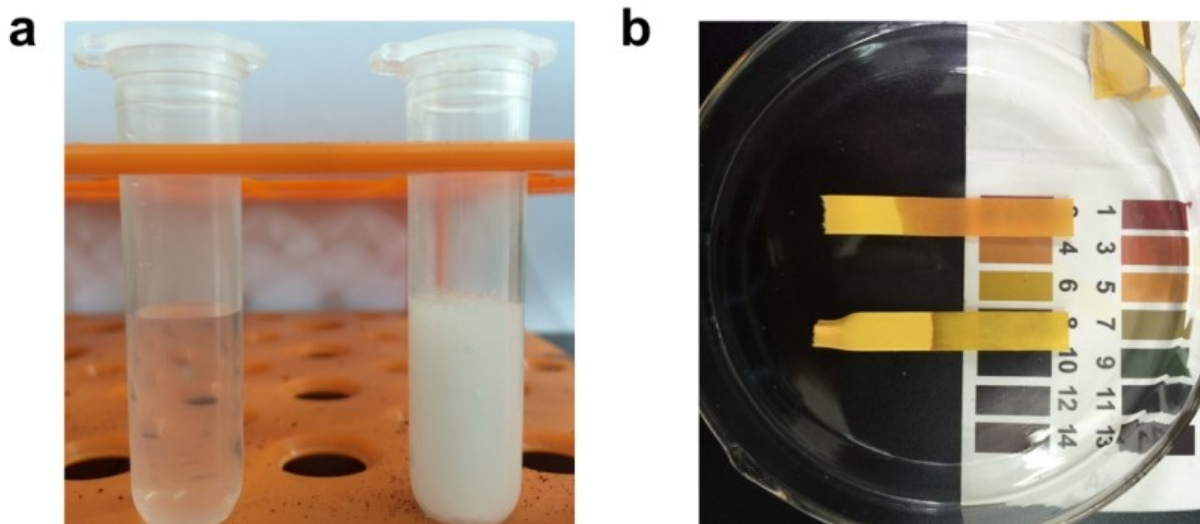**Figure S1.** NMR and IR spectrum of MMZ and IQL.

Figure S2. (a) A clear solution of the gas produced by heating in H_2O (left) and a white precipitate formed after the addition of silver nitrate (right). (b) The pH of the gas produced by heating in H_2O (top) and the pH of purified water (bottom).
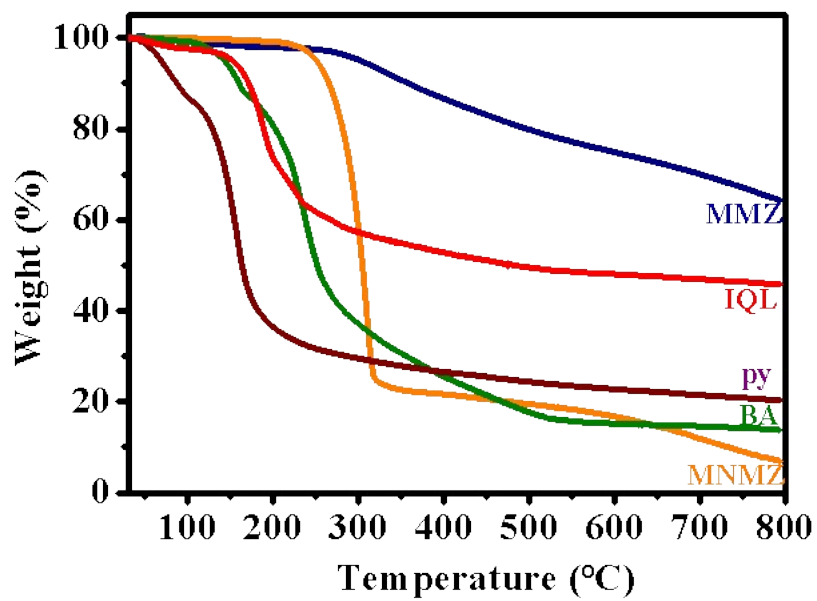
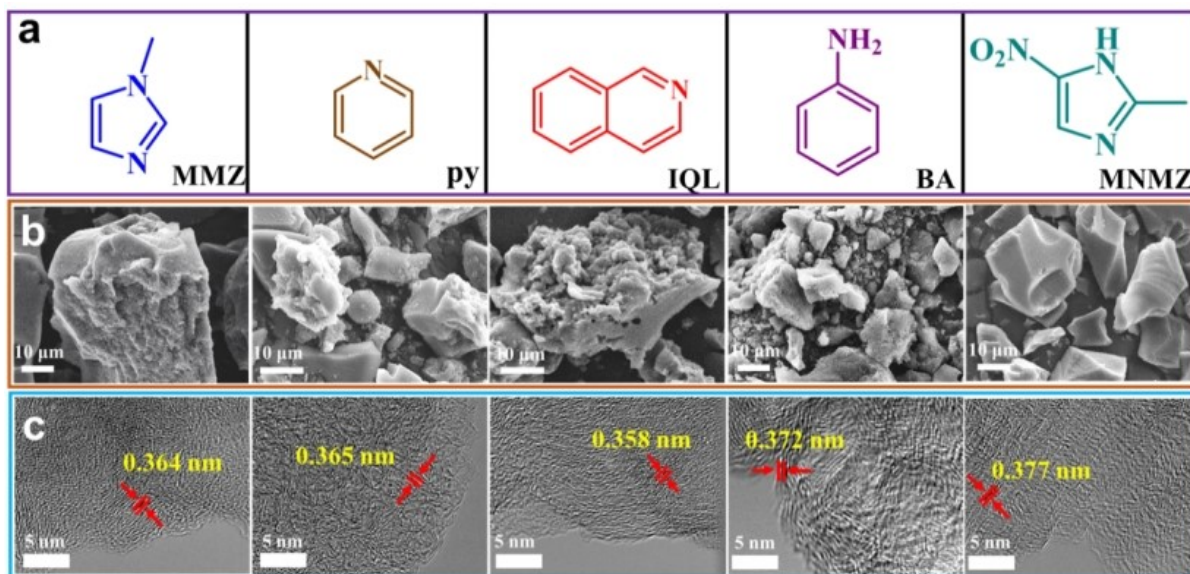**Figure S3.** TG analysis of MMZ, IQL, BA, MNMZ and py.

Figure S4. Characterizations of related carbon materials derived from five different precursors. (a) Structural formula; (b) SEM and (c) HRTEM image.

As can be seen from the molecular structure in Figure S4a, various electrophiles (1-methylimidazole, pyridine, isoquinoline, aniline, 2-methyl-5-nitroimidazole) have different molecular configurations, which have a crucial impact on the performance of the material. The morphological features of HCs based on polymers can be observed through the scanning electron microscopy (SEM) image in Figure S4b. MMZ, IQL, BA, and MNMZ all mainly displayed the morphology of chunk-like material with a diameter between 8 and 15 μm. High resolution transmission electron microscopy (HRTEM) images reveal the detailed microstructure of HC materials obtained above. It can be seen from Figure S4c that the interlayer distances of 1-methylimidazole with pendant five-membered ring structure and pyridine with six-ring structure are 0.364 and 0.365 nm, respectively. However, the interlayer spacing is much smaller than that of the HC corresponding to 2-methyl-5-nitroimidazole with two side chains (0.377 nm), indicating that the side chains can effectively widen the interlayer spacing of HC materials. The HC materials synthesized with pyridine and aniline as

precursors can also confirm this view, and the corresponding interlayer spacings are 0.365 and 0.372 nm, respectively. In addition, we find that the HC structure generated from isoquinoline has the smallest interlayer spacing among all the generated materials, and its interlayer spacing is only 0.358 nm. This is because the raw material structure itself tends to be a planar structure, which makes it have stronger interlayer force after the polymerization reaction and more ordered in a short range. Therefore, its interlayer spacing after carbonization is significantly smaller than that of other HC materials. Combined with HRTEM, the interlayer spacing is positively correlated with the pore volume of the material (Table S5). Because MNMZ has more branched chains, the intermolecular force is relatively weak when the polymer is formed, and it has poor thermal stability (Figure S3). Therefore, it is easy to decompose during the heat treatment process, and a large amount of gas is generated, resulting in a large specific surface area and widely pore size distribution. This is consistent with the phenomenon observed in FTIR (Figure S6).
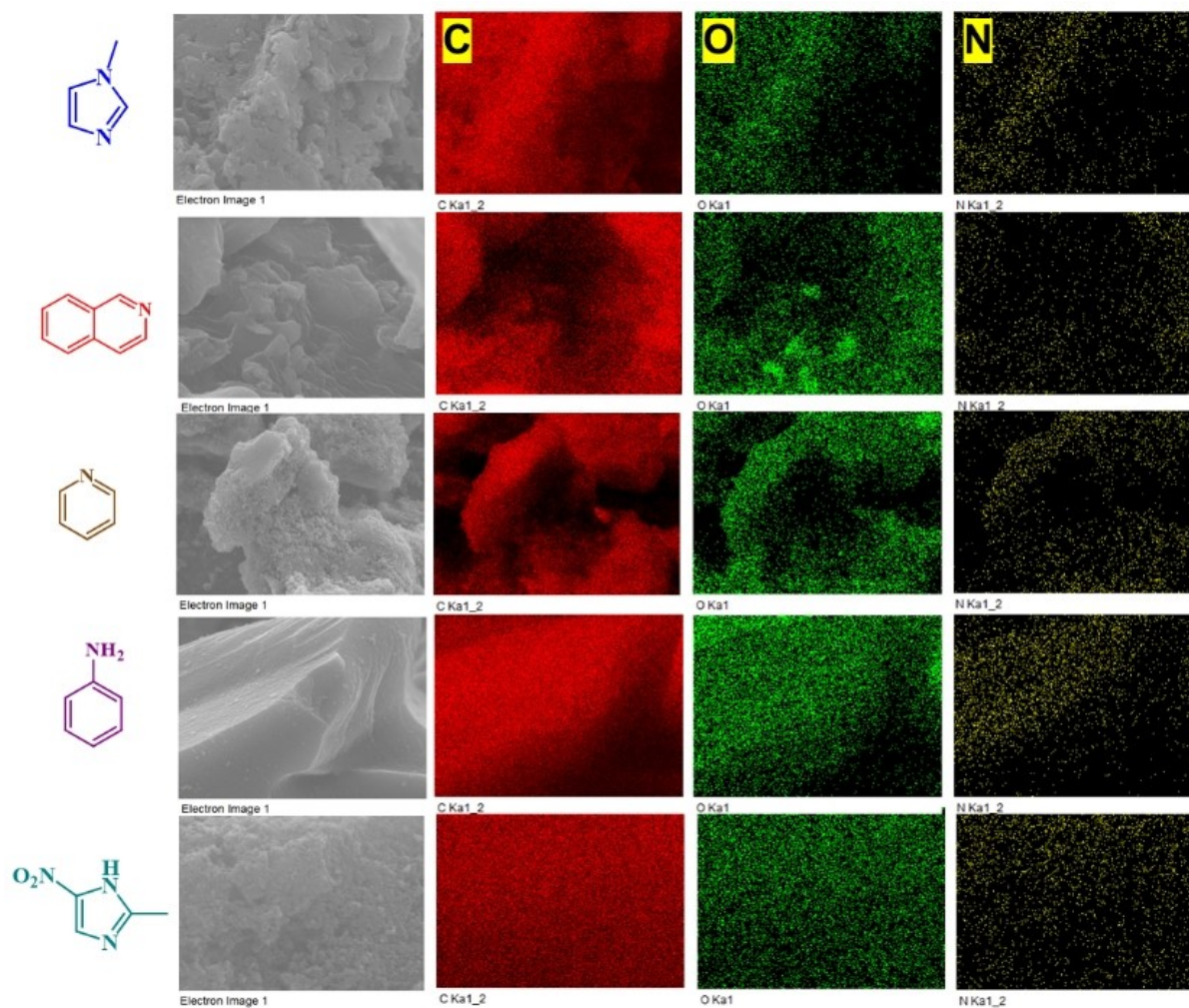
Figure S5. EDS mapping of MMZ, IQL, py, BA and MNMZ (from top to bottom).

As can be seen from the EDS mapping in Figure S5, nitrogen and other elements are uniformly distributed. In addition to the blocky morphology, the sample of py was accompanied by a small amount of spherical morphology. Through molecular simulation, with the addition of nucleophiles of different configurations, the spatial structure of the polymer also changes from two-dimensional to three-dimensional, and the main research focuses on the ring structure and branched chain of nucleophiles. The uniform distribution of various elements is seen from the EDS map, proving the consistency of the reaction.
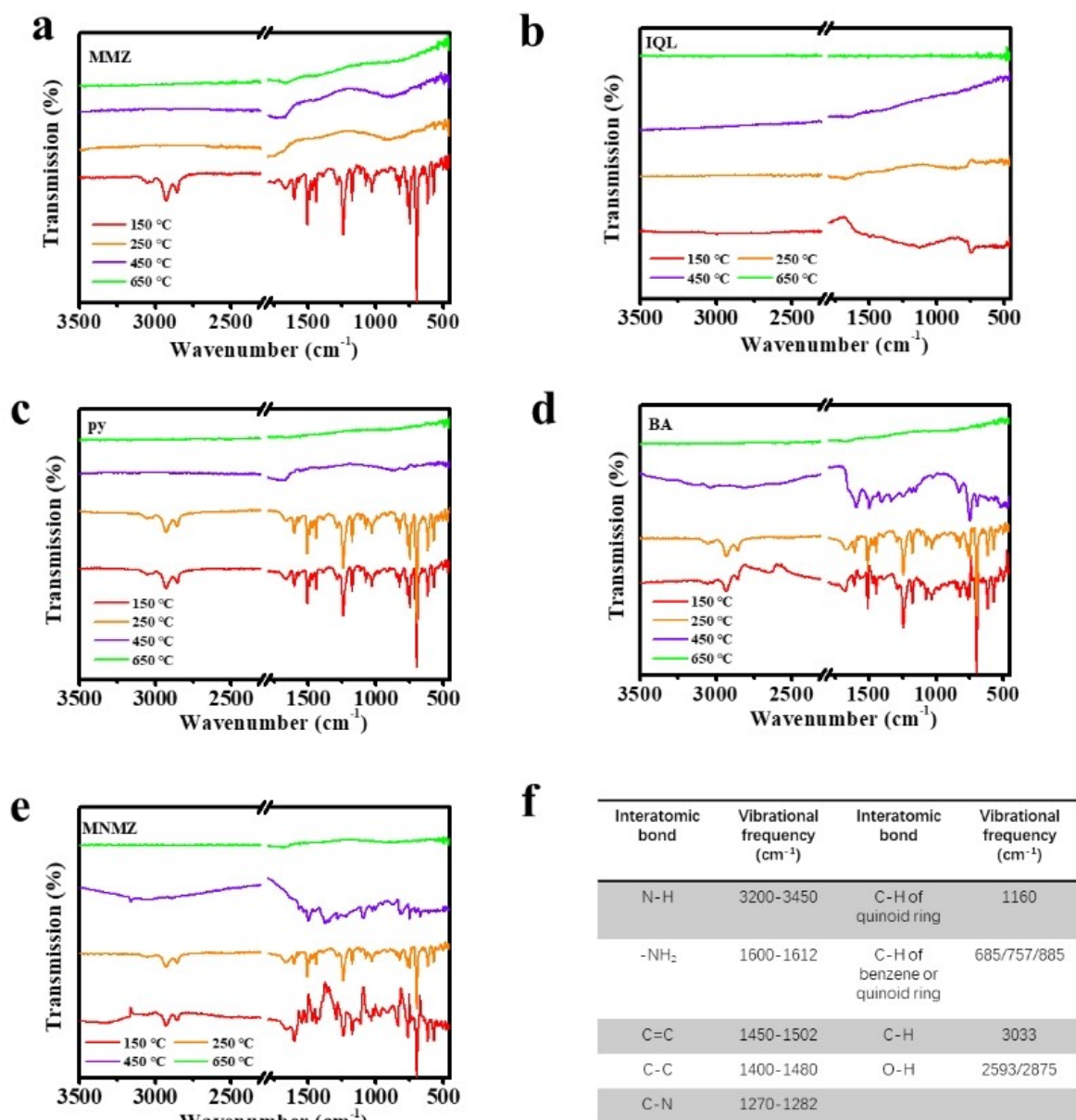
Figure S6. FTIR spectra of (a) MMZ (b) IQL, (c) py, (d) BA and (e) MNMZ. (f) FTIR vibration modes and correspondent peak positions.

FTIR spectra was further conducted to investigate the interaction between HCBD and nitrogenous compounds, as show in Figure S6a-6e, and the FTIR vibration modes and correspondent peak positions are summarized in Figure S6f. For the pure HCBD and nitrogenous compounds composite, there co-exist some typical characterization peaks at

around 1450-1502 cm^{-1}, 1400-1480 cm^{-1}, 1270-1282 cm^{-1}, which are referring to C=C, C-C, C-N/C-O bonds. Strong peaks at 1631 cm^{-1} and 439 cm^{-1} may be ascribed to C=C-C=C and C-Cl stretching vibration respectively. The absorption signals at 1000-1350 cm^{-1} stretching vibration of C-N. The peak at 880-680 cm^{-1} is attributed to bending vibration of C-H. It confirms successful inheritance of functional groups in HCBD-nitrogenous compounds from nitrogenous compounds molecular units. Compared with MMZ and IQL, MNMZ, py, BA requires higher temperature for carbonization. All samples have completed the polymerization carbonization process at 450 °C. Therefore, MMZ and IQL carbonized at low temperature possess higher thermal stability, which is also consistent with the thermogravimetric results (Figure S25).
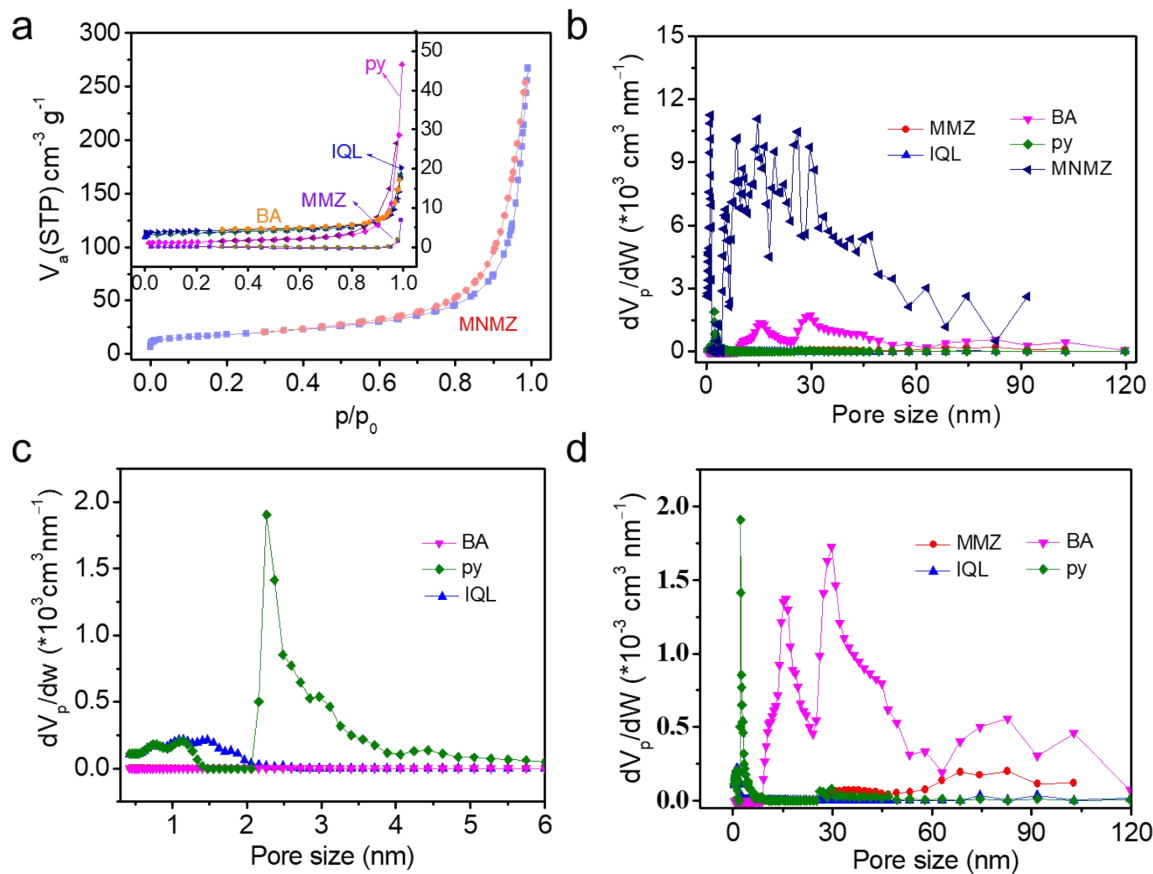
Figure S7. (a) N_2 adsorption/desorption isotherms, (b) pore size distribution; (c) and (d) the enlarged figure showing the small mesopores of MMZ, IQL, py, BA and MNMZ.

The surface area and pore size distribution of the samples using nitrogen absorption and desorption test are displayed in Figure S7. The surface areas of MMZ, py, IQL, BA, and MNMZ are 0.404, 5.27, 0.739, 5.51 and 68.1 m^2 g^{-1}, respectively.

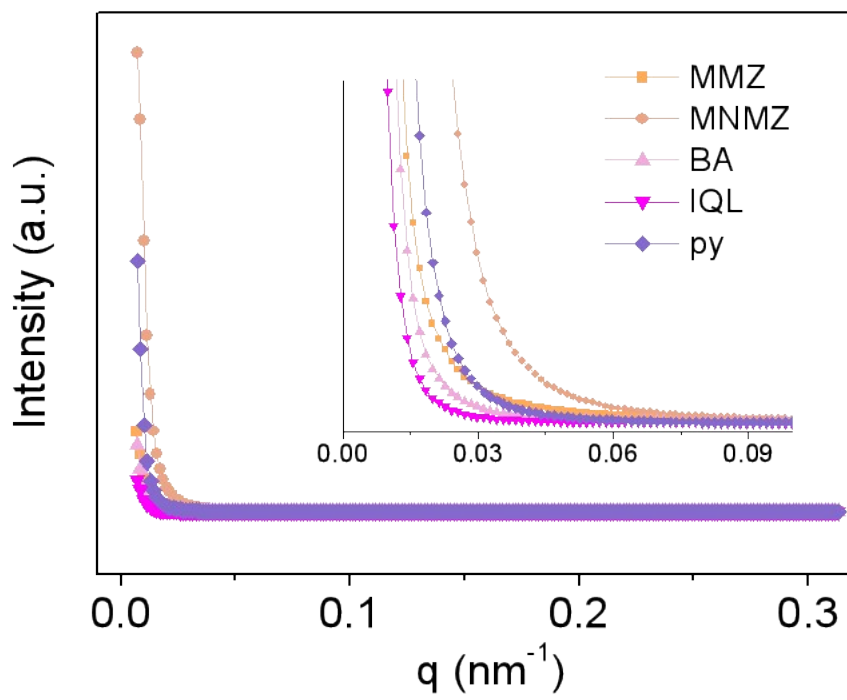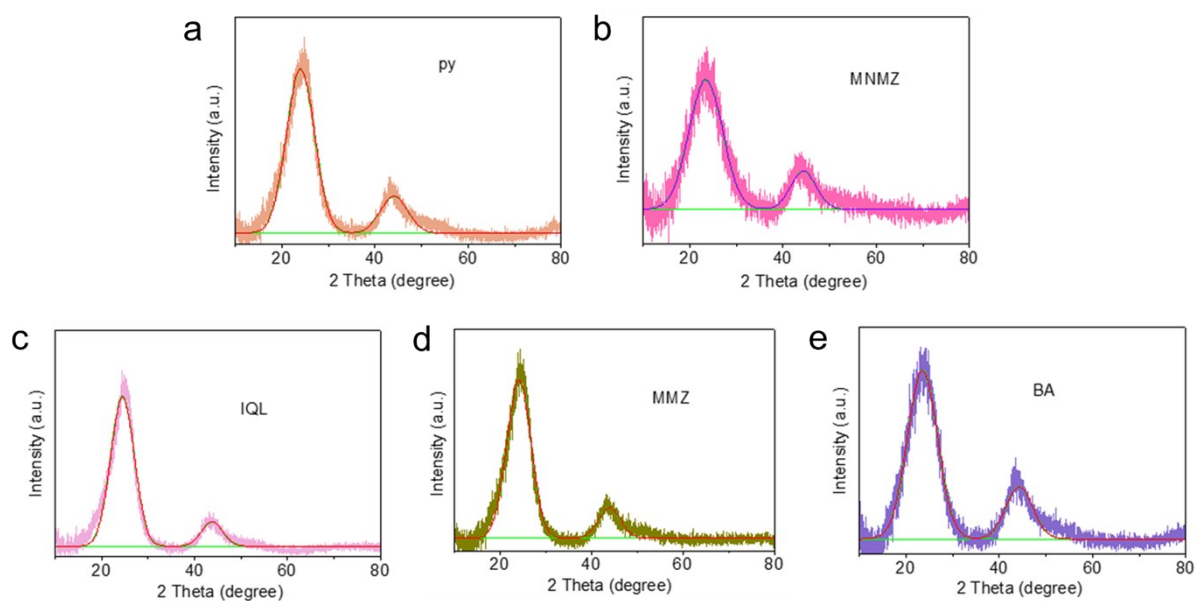**Figure S8.** SAXS graph of MMZ, IQL, py, BA and MNMZ.

Figure S9. Fitted XRD spectra of py, MNMZ, IQL, MMZ and BA.

Parameters such as L_a and L_c calculated based on formula 1 and 2 are very important for evaluating the dispersion region structure. Therefore, the accuracy of peak position directly affects the accuracy of its structural parameters. In order to obtain more accurate peak positions and half-peak widths in the XRD pattern, the data were fitted by Gaussian fitting method. The peak positions and half-peak widths after fitting were shown in Table S2, and the fitting spectra were shown in Figure S9.
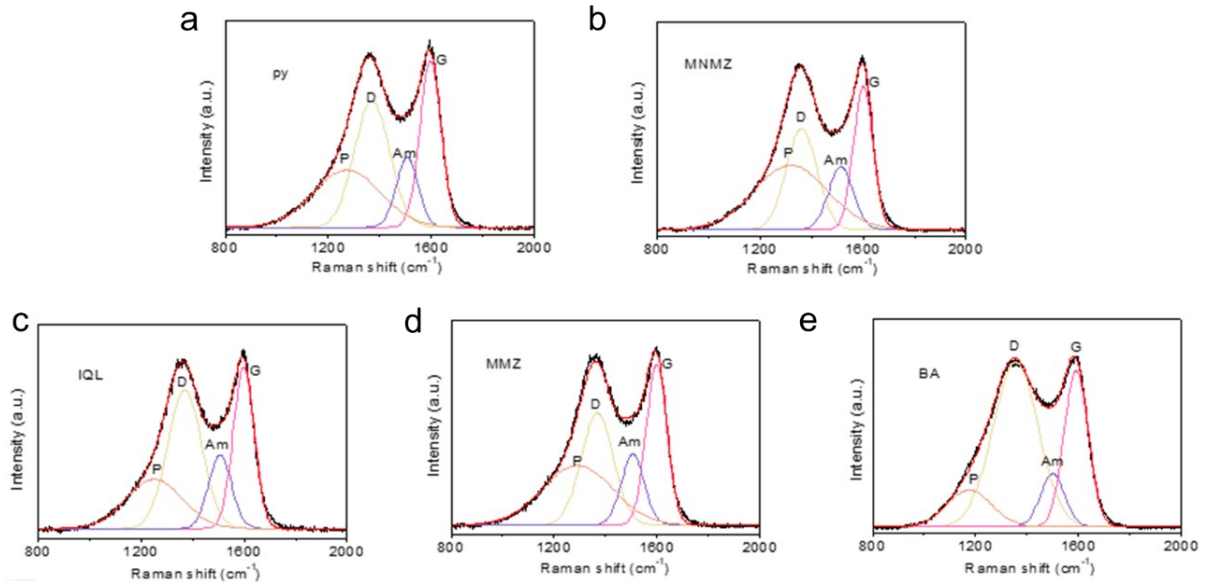
Figure S10. Fitted Raman spectra of py, MNMZ, IQL, MMZ and BA.

The in-plane coherence length of the graphitic domains, La, can be estimated from Raman spectra according to following equation: L_a (nm) = (2.4x10^{-10}) λnm^4(I_D/I_G)$^{-1}$,[17-19] where λnm is the laser wavelength, 532 nm.
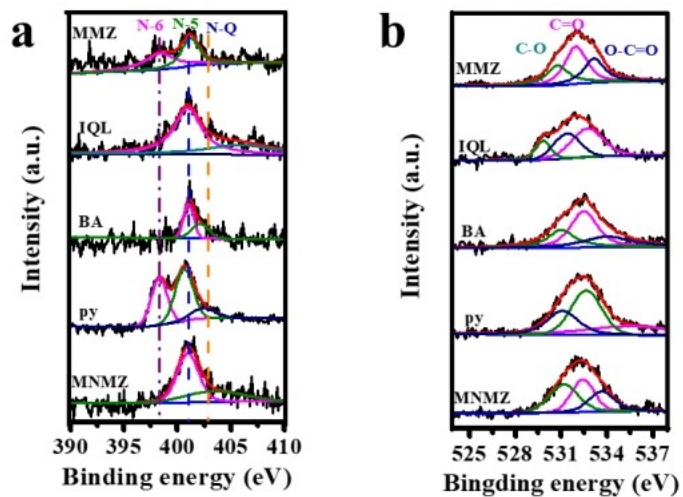
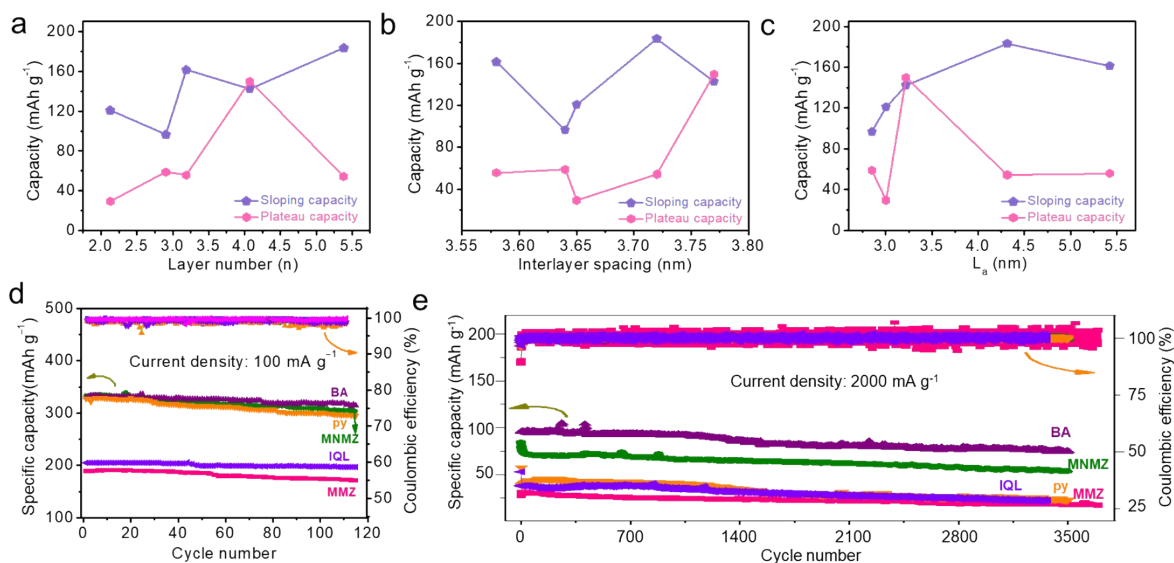**Figure S11.** High-resolution XPS spectrum of (a) N1s and (b) O1s[20].

Figure S12. Electrochemical performance characterization of HC obtained by dechlorination polymerization (MMZ, py, MNMZ, BA and IQL). Relationship between sloping capacity-plateau capacity and the (a) layer number, (b) d, and (c) L_a. (d) The cycling performances at 100 mA g^{-1}. (e) Long-term cycling performance.

All samples show good capacity retention at both low rate (100 mA g^{-1}) and high rate (2000 mA g^{-1}) cycling conditions with 0.005%~0.017% and 0.036%~0.081% capacity decay per cycle, respectively (Figures S12d-S12e and S25). As we describe, modifying the electronegativity of the polymerized nitrogen-containing molecules by modulating the branched groups can further increase the graphite interlayer spacing and increase the plateau capacity. Meanwhile, we found that it is not a single condition (such as L_a, L_c and d, etc.) but the joint action of the graphite crystallite structure and the amorphous structure that determines the final properties of HC. Since the diameter of Na ions is only 0.196 nm, Na ions will inevitably be adsorbed between the graphite layers, and the increased interlayer spacing makes Na ions easier to enter, resulting in an increase in the adsorption capacity.
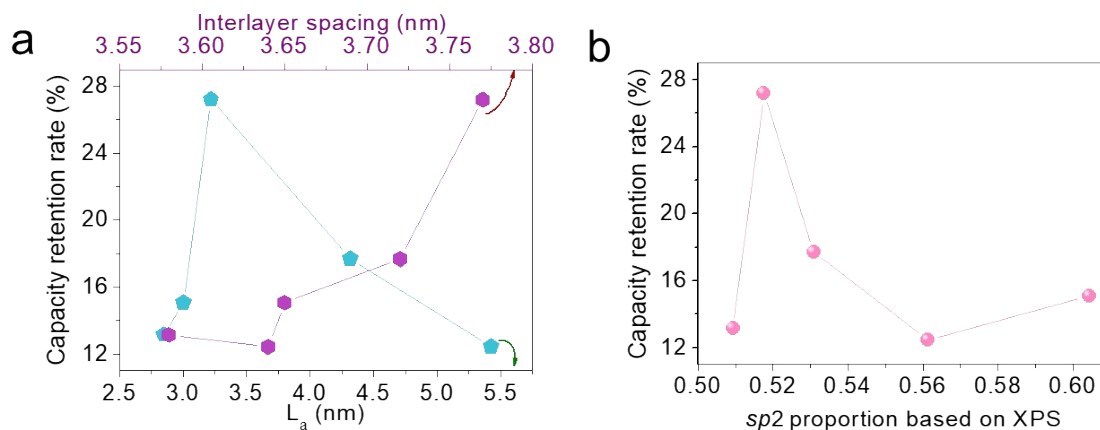
Figure S13. Relationship between capacity retention and the (a) interlayer spacing and L_a, and (b) *sp2* proportion based on XPS.

In addition, L_a and d also affect the rate performance of the material, as shown in Figure S13a. When La is less than 3.3 nm, it is positively correlated to the rate behavior, but when L_a is larger than 3.3 nm, it is not conducive to the rate performance of the material as it increases. The capacity retention increases with the increase of d, which indicates that a large interlayer spacing is beneficial to improve the rate performance of the material. The increase in the length of L_a makes the van der Waals force, electrostatic force, π-π interaction, hydrogen bond interaction and other forces between the graphite layers stronger, inducing in a decrease in the interlayer spacing of the graphite layer, which hinders the intercalation process of sodium ions, resulting a reduction of plateau capacity and rate performance. While the plateau capacity and capacity retention exhibited the best performance at the *sp2* content of 52% (Figure S13b). Even at a rate of 2000 mA g^{-1}, the initial capacity value of 27.2% is still achieved. Among them, MMZ with the least electronegativity has short graphitic domain structures with L_a of 2.85 nm and L_c of 1.04 nm. In contrast, the most electronegative IQL with a significant degree of graphitization, L_a and L_c are 3.00 nm and 0.78 nm, respectively,

and the graphite stack is 2 layers. After fully balancing the reversible sodium storage performance and rate performance, the optimal graphitization ratio is 52%−53%.
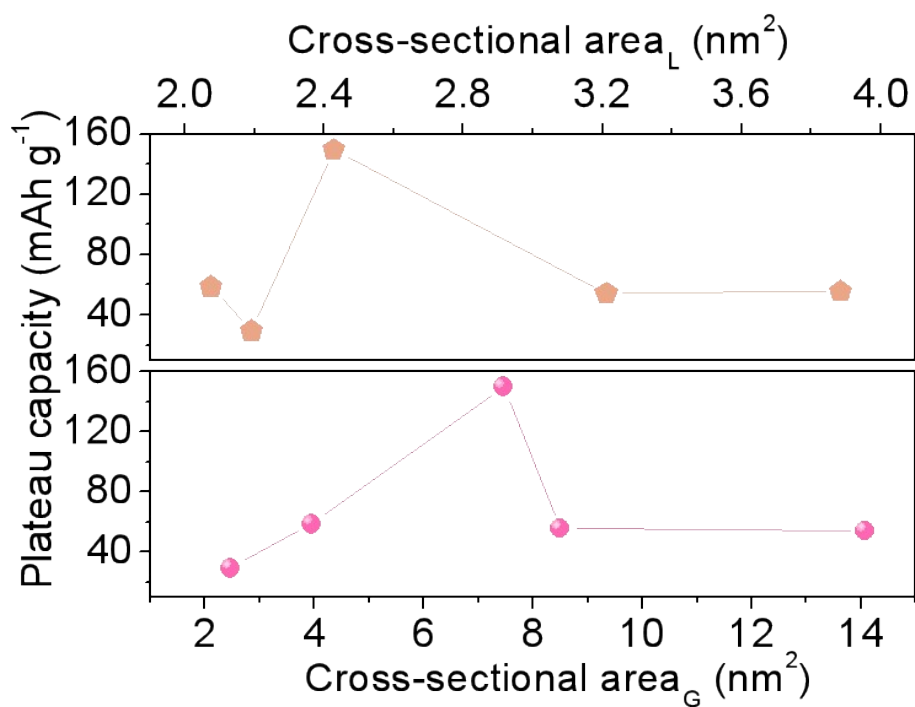
Figure S14. Interlayer diffusion cross-sectional area and graphite crystallite cross-sectional area versus plateau capacity.
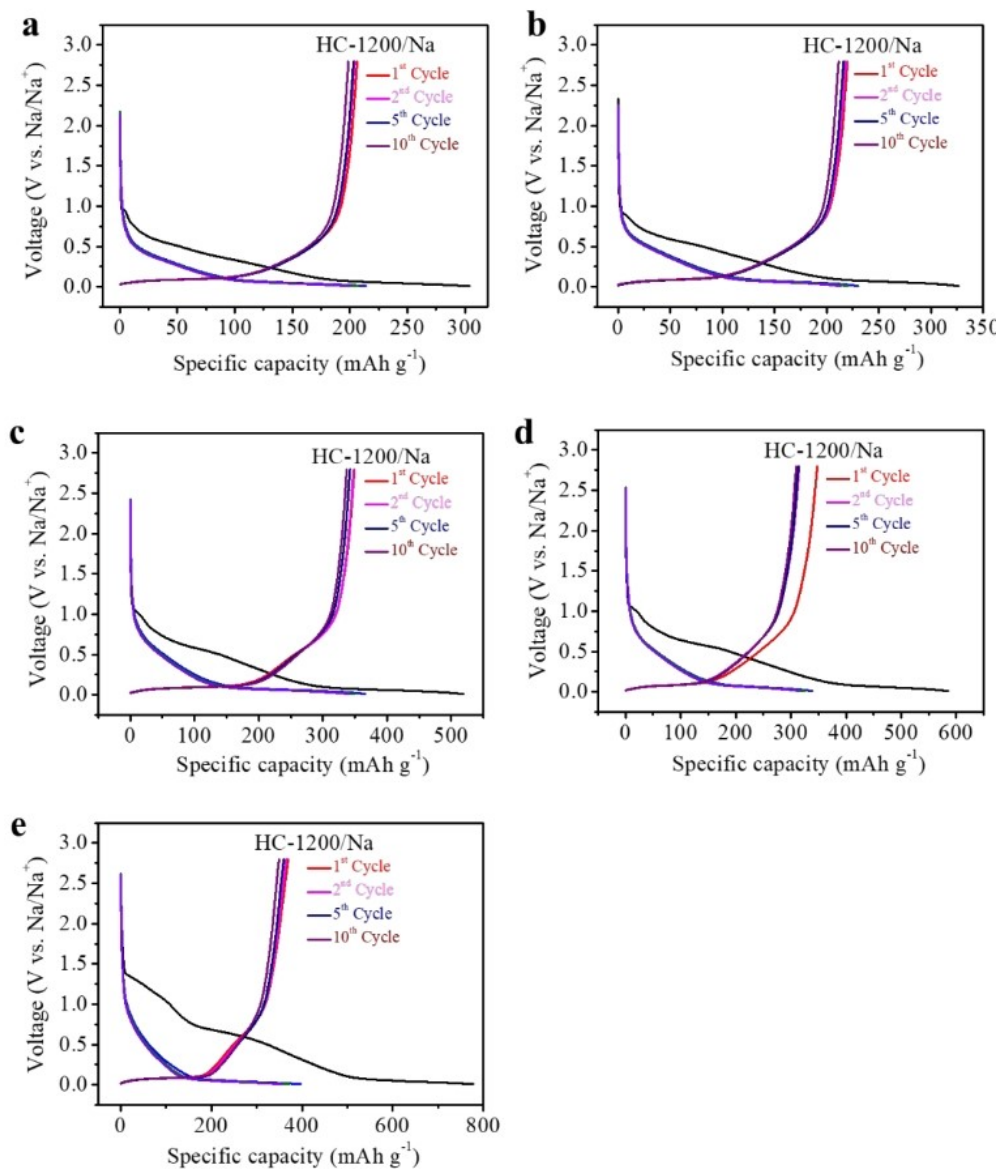
Figure S15. The discharge-charge profiles at 1st, 2nd, 5th and 10th cycle of HC obtained by dichlorination polymerization (a) MMZ, (b) IQL, (c) BA, (d) py and (e) MNMZ.

The rate performances of the samples are also compared with representative researched carbon anodes (Figure S26). In contrast to the rapid capacity decrease for most carbon anodes, BA and IQL exhibit much slower capacity deterioration, indicating a favorable high-rate performance for the BA.

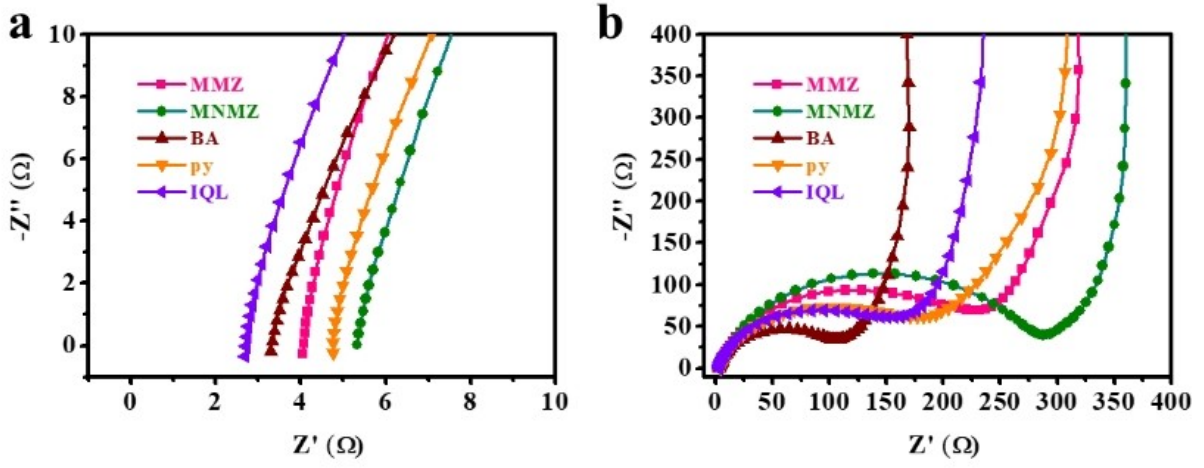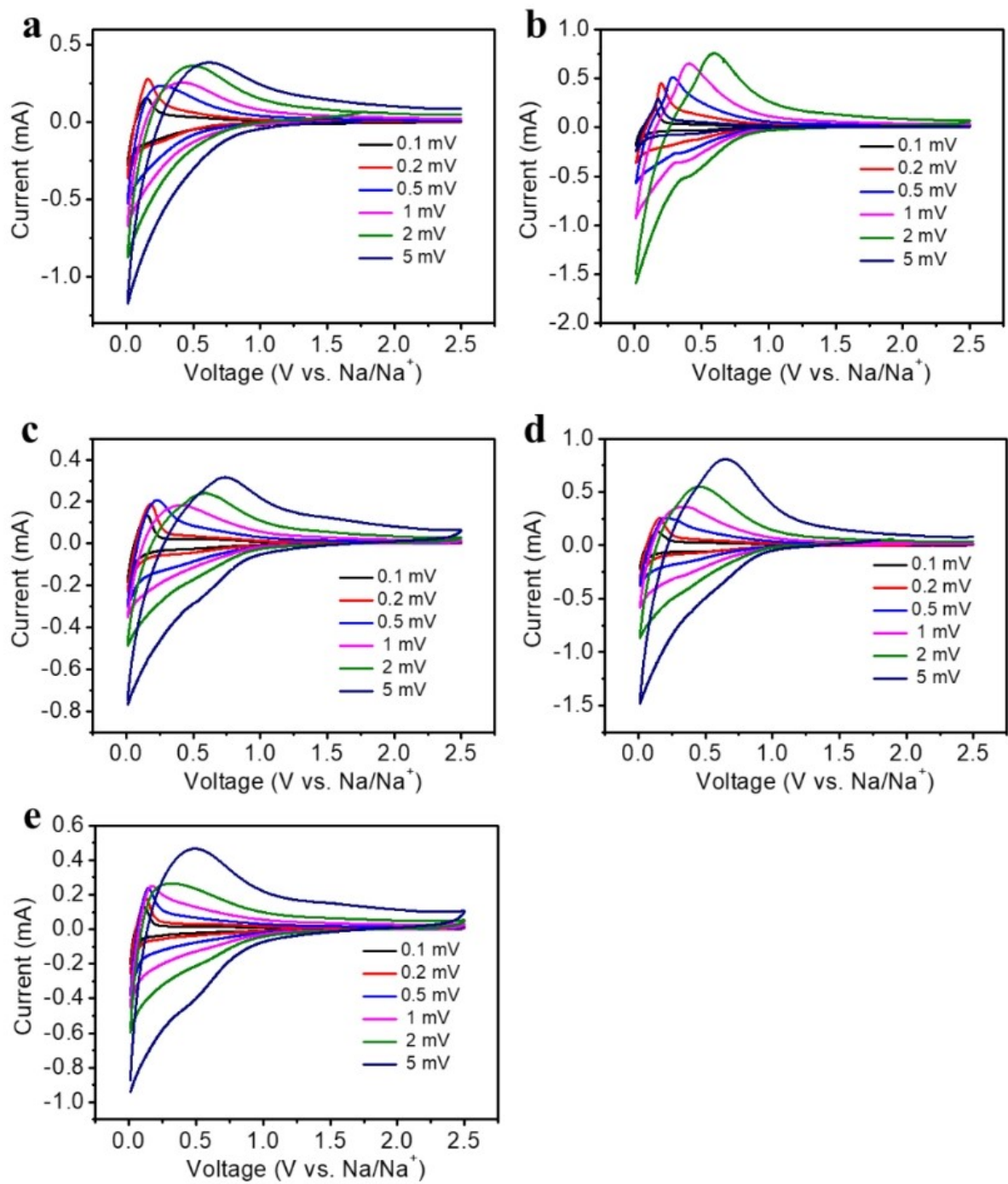**Figure S16.** (a) and (b) depict the enlarged Nyquist plots of the electrodes.

Figure S17. CV curves at different scan rates (0.1–5.0 mV s^{-1}) of HC obtained by dichlorination polymerization (a) MMZ, (b) IQL, (c) BA, (d) py and (e) MNMZ.
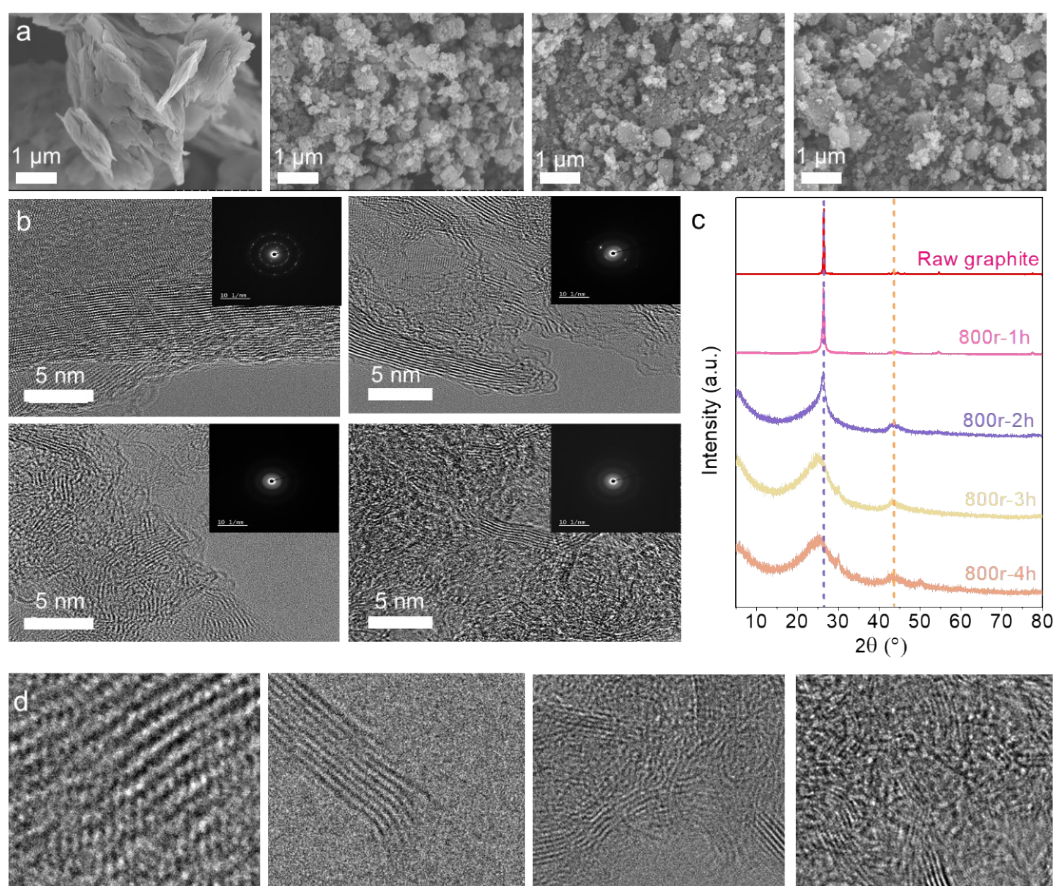
Figure S18 SEM (a), HRTEM (b (inset: SAED of 800r-Xh), d), XRD (c) images of graphite treated with different ball milling time at 800r/min.

In order to explore the influence of transition layer on sodium ion diffusion, we used graphite as raw material and obtained a series of materials (respectively denoted as 800r-Xh, X=1, 2, 3, 4) by controlling different ball milling times at the speed of 800r/min. With the extension of ball milling time, the long range ordered structure of graphite is gradually destroyed. Through SEM, the macroscopic structure of the material can be obtained, showing gradually smaller particles (Figure S18a). HRTEM can see that a long-range ordered structure is gradually destroyed (Figure S18b). Selected area electron diffraction (SAED) and XRD can see that graphite is gradually transformed into an amorphous form (Figure S18c). As shown in Figure S18d, a transition layer structure appears at the fracture after ball milling.

Figure S19. Electrochemical properties of different carbon materials in ester electrolyte. Comparison of the discharge-charge profiles in the first cycle (a) and second cycle (b). (c) The rate capability from 50 to 2000 mA g^{-1}. (d) Long-term cycling performance at 1 A g^{-1}.

With the extension of ball milling time, the material defects are more abundant, and the exposed active sites can significantly improve the electrochemical performance of the material. In the ester electrolytes, the defects increase gradually with the increase of milling time, and the rate performance is better. The 800r-4h sample still has a capacity of ~170 mAh g^{-1} at the current density of 2 A g^{-1}, and remains 72.3% for 2000 cycles at the current density of 1 A g^{-1}.
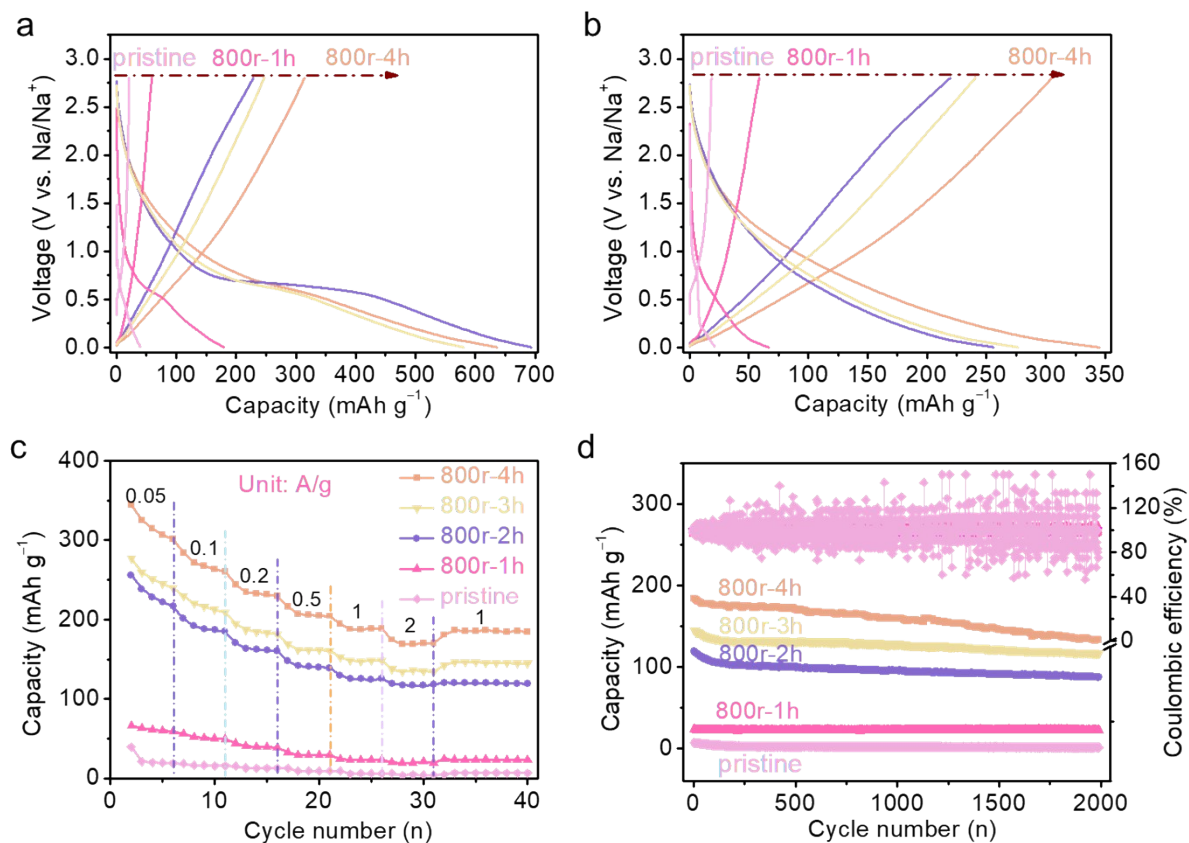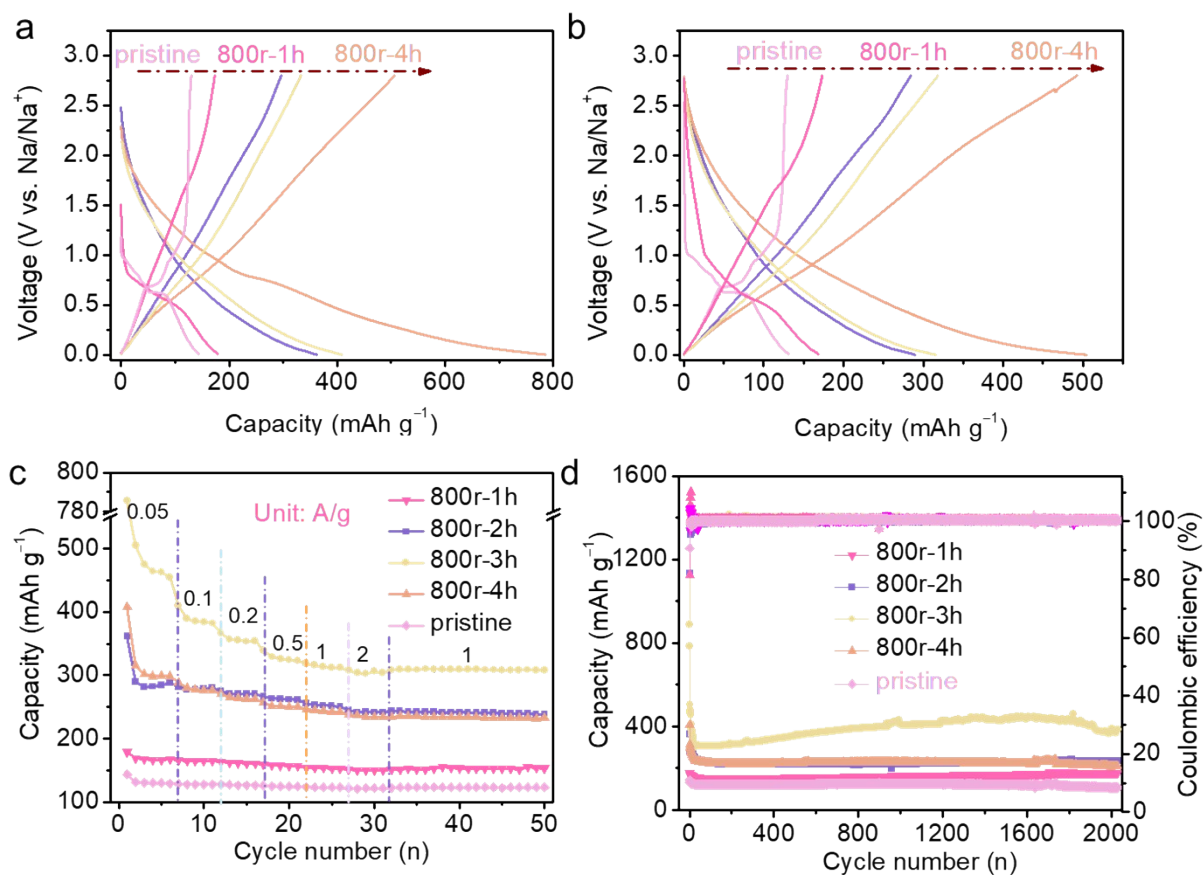
Figure S20. Electrochemical properties of different carbon materials in ether electrolyte. Comparison of the discharge-charge profiles in the first cycle (a) and second cycle (b). (c) The rate capability from 50 to 2000 mA g^{-1}. (d) Long-term cycling performance at 2 A g^{-1}.

In ether hydrolysates, due to the existence of co-embedding process, the rate performance is not the better the more defects, 800r-3h sample still has a capacity of ~ 300 mAh g^{-1} under the current density of 2 A g^{-1}, and the current density of 1 A g^{-1} for 2000 cycles still maintains 76.3%.

31
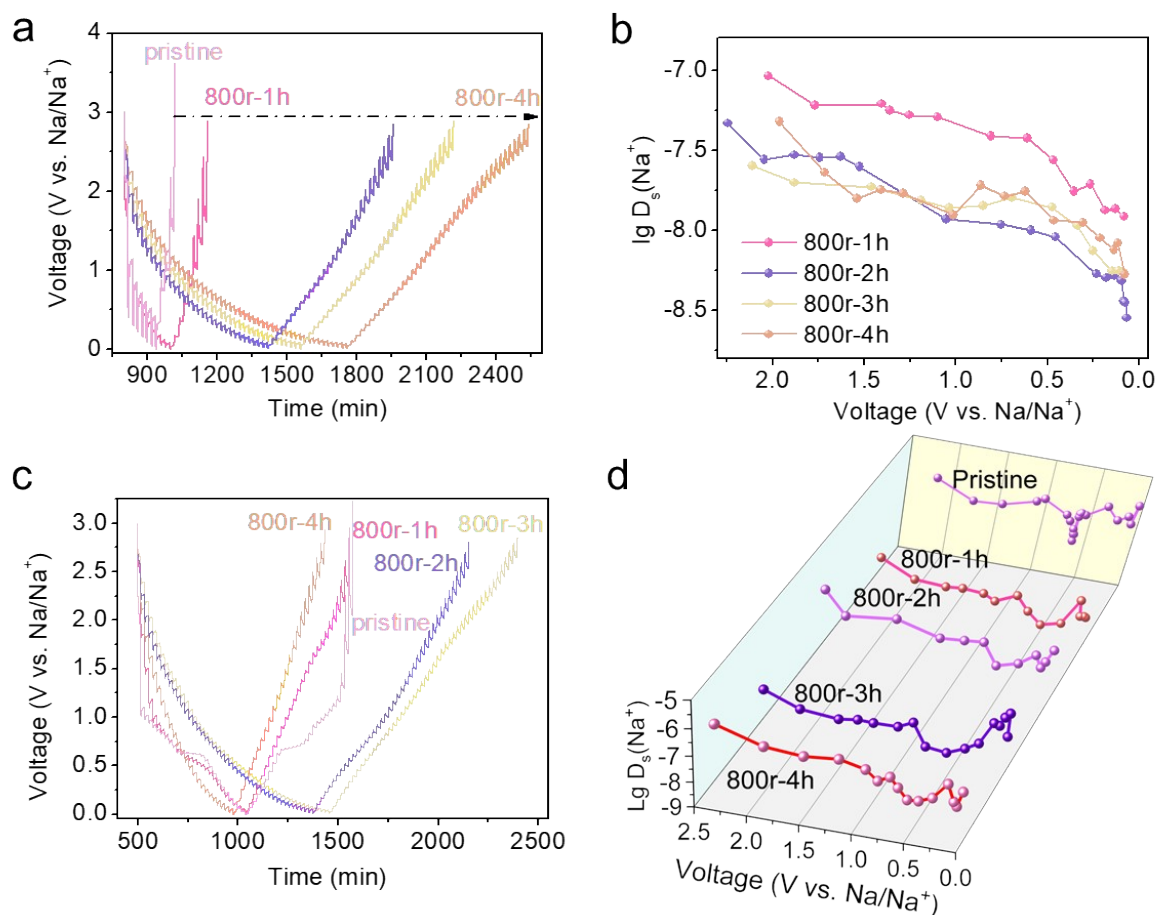
Figure S21. GITT and sodium diffusion coefficients of different carbon materials prepared in ester (a, b) and ether electrolyte (c, d).

It can be seen from GITT and sodium ion diffusion coefficient that the sodium ion diffusion coefficient decreases in both esters and ethers. There was only an order of magnitude reduction in ester electrolytes and no recovery. In the ether electrolyte, the diffusion coefficient decreases first and then increases, and the potential is about 0.7 V, which is consistent with the embedding potential of sodium ion in graphite. As we know, in the ester electrolyte, graphite is unable to store sodium ions, so only the accumulation of sodium ions in the transition layer occurs. However, in ethers, sodium ions can be stored in graphite by solvation, so the phenomenon of sodium ion diffusion coefficient will be increased.

32
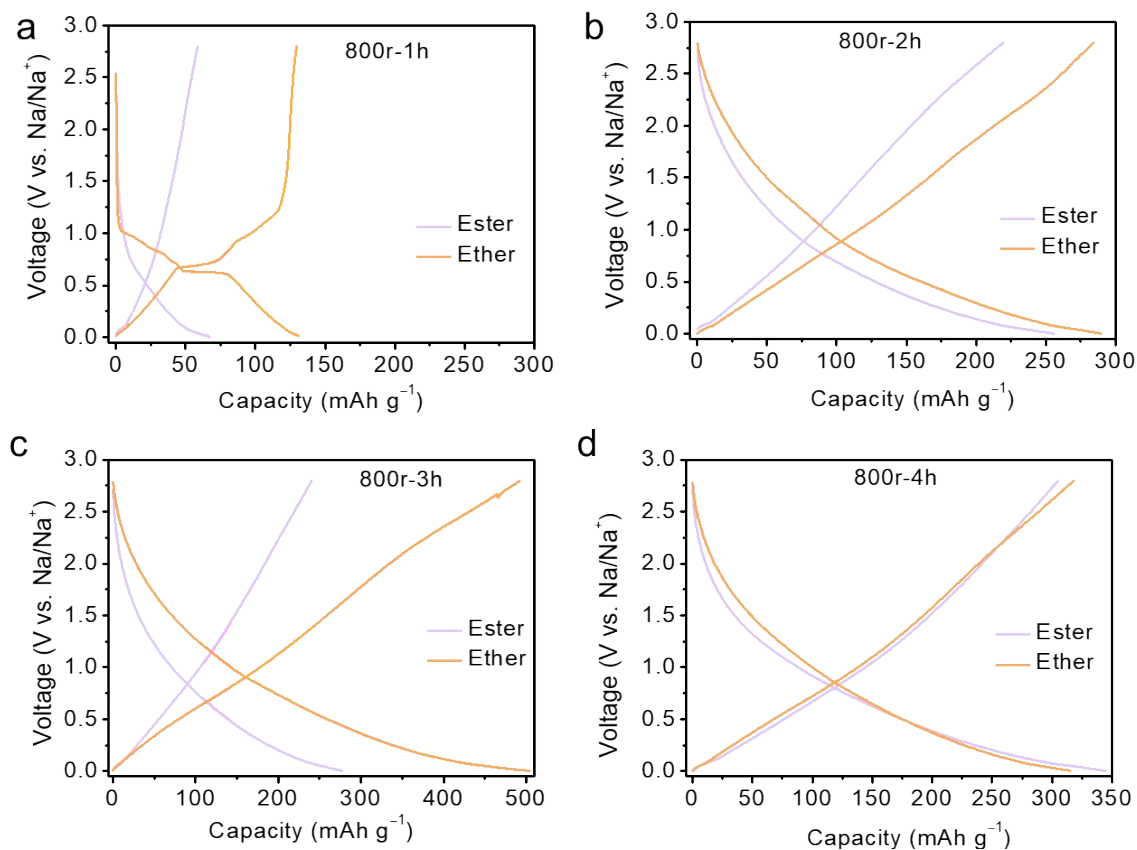
Figure S22. Comparison of electrochemical properties of different carbon materials prepared in ester and ether electrolyte. (a) 800r-1h, (b) 800r-2h (c) 800r-3h (d) 800r-4h.

Comparing the graphite materials treated with different ball milling times, it can be found that the capacity of 800r-Xh (X= 1,2, 3) in ester analogy is small in ether electrolyte solution, indicating that the reduction of graphite fragment size can increase the storage capacity of sodium ions (Figure S22a-c). With the destruction of the long-range ordered structure of graphite, the capacity of 800r-4h sample eventually tends to be the same in the two electrolytes, indicating that the material's sodium storage is entirely dependent on the defect sites generated by ball milling (Figure S22d).
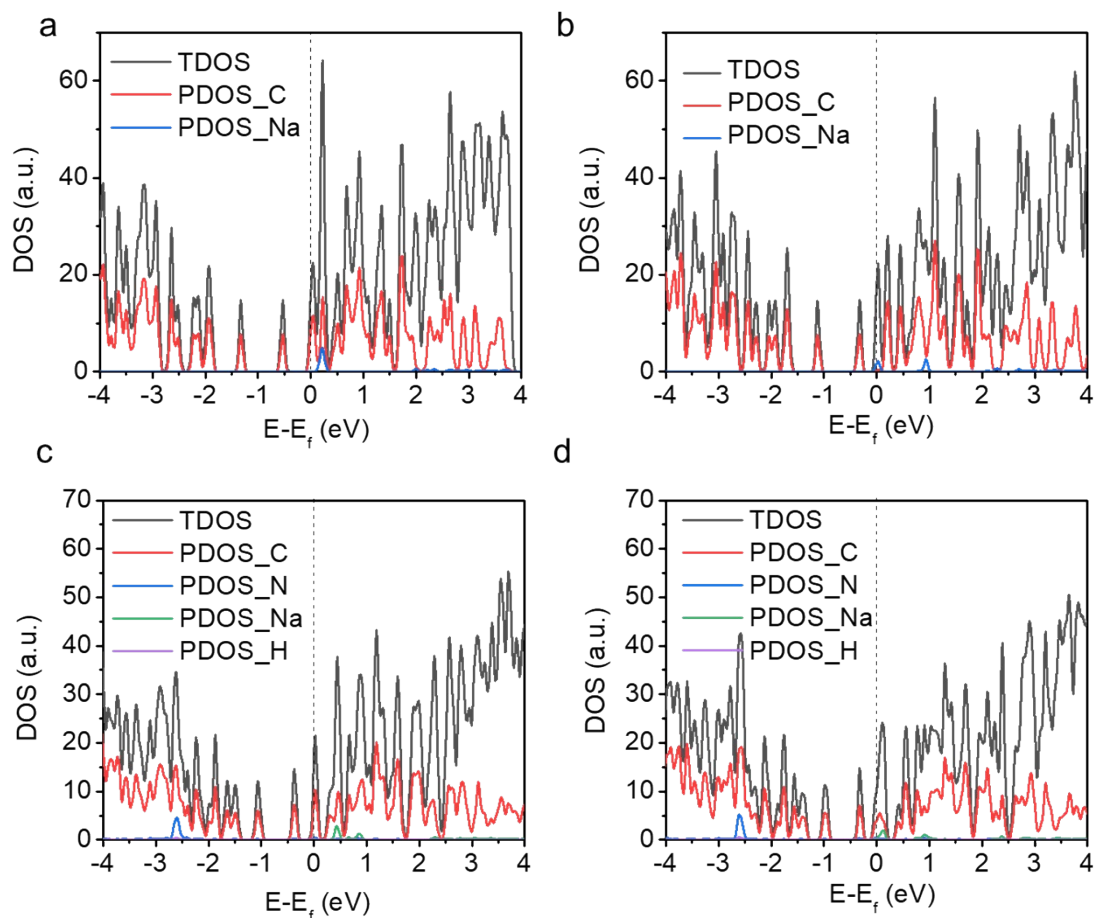
Figure S23. DOS of 2Na and 2Nas on the single-layer graphene (a, b) and NGN (c, d), which have contributions from 3s-electron of Na (2Na and 2Nas correspond to two sodium atoms alone and formed 2Na cluster, respectively). The Fermi level is set to zero.
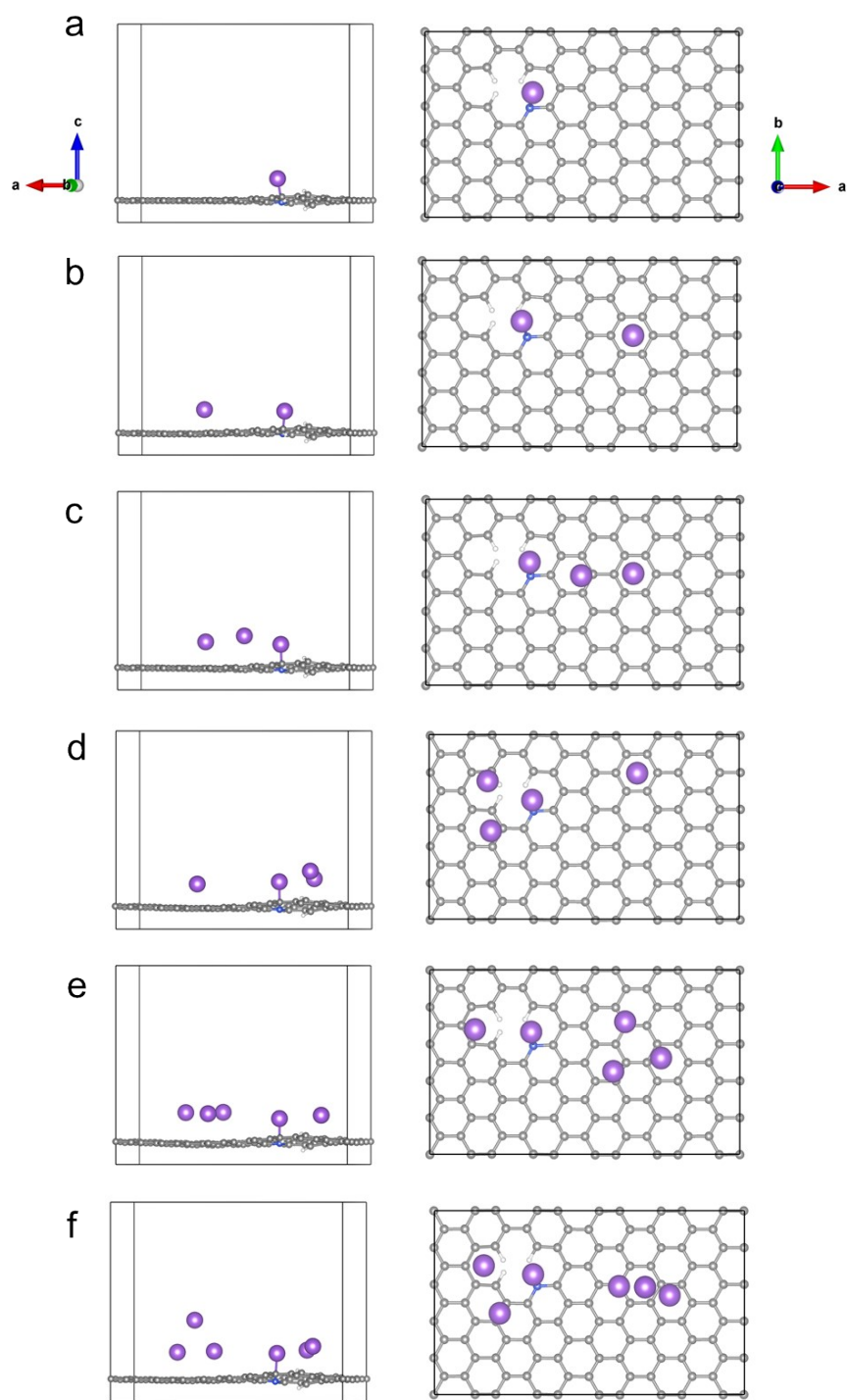
Figure S24. The schematic illustration for how the Na-Na, G-Na and NGN-Na interactions determine sodium ions storage states on the diffusion region (Na atoms and Na clusters are drawn as red and green spheres, respectively).
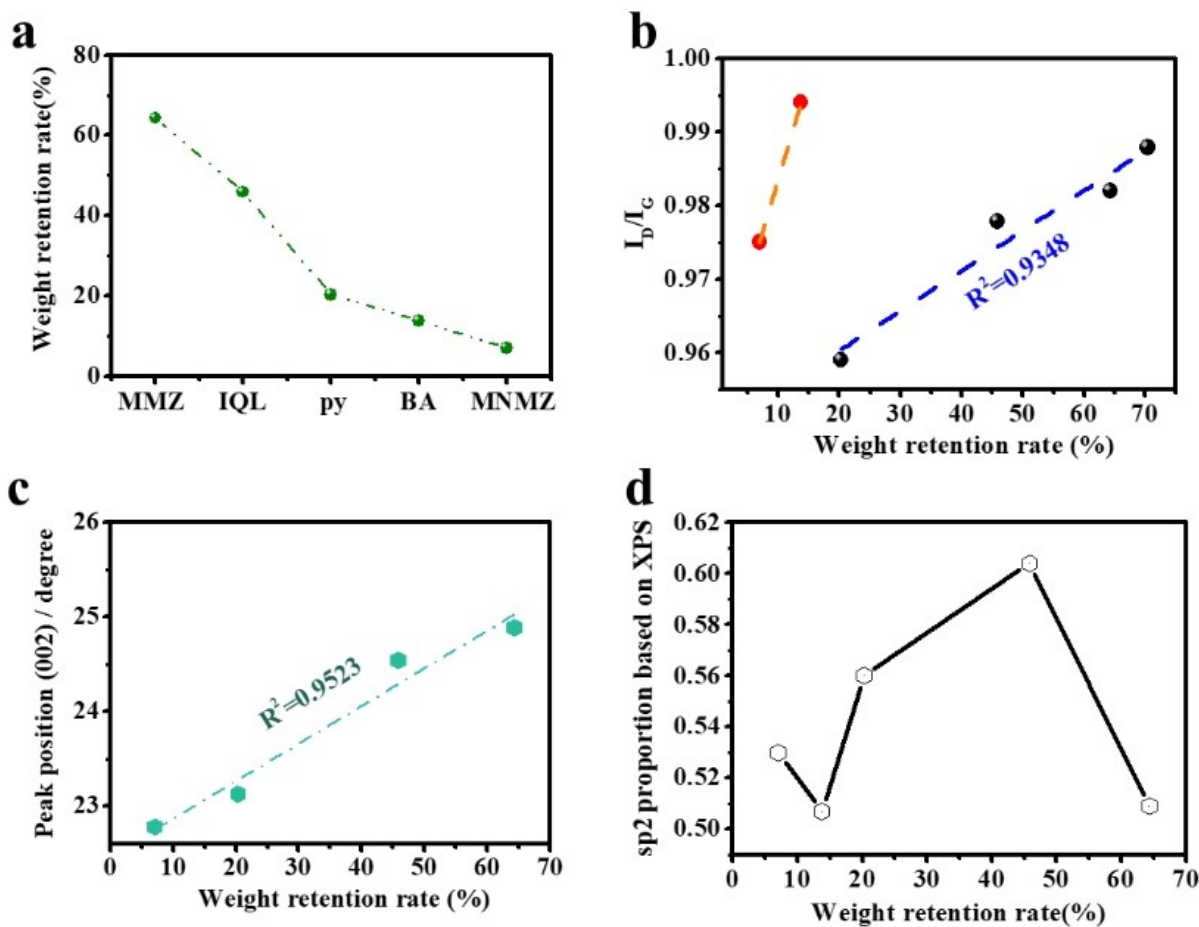
Figure S25. Relationship between weight retention rate and (a) electronegativity of nitrogen atom, (b) I_D/I_G, (c) peak position (002) and (d) $sp2$ proportion based on XPS.

By analyzing the proportion of samples under nitrogen protection, we found that the increase in the degree of polymerization of the material will make the material more stable, and the degree of polymerization of the material is related to the electronegativity of the nucleophile participating in the reaction (Figure S25a). The difference in electronegativity of the nucleophile affects the thermal stability of the polymer and thus the degree of graphitization of the material upon carbonization. The more weight loss of the material, the lower the degree of graphitization (Figure S25b). The increase in the degree of graphitization

is also accompanied by a decrease in the interlayer spacing, and the (002) diffraction peak shifts to high angles (Figure S25c). Thermogravimetric analysis showed that a suitable weight loss rate would make the material exhibit a higher degree of amorphousness, thereby enhancing the electrochemical energy storage behavior of the material (Figure S25d).
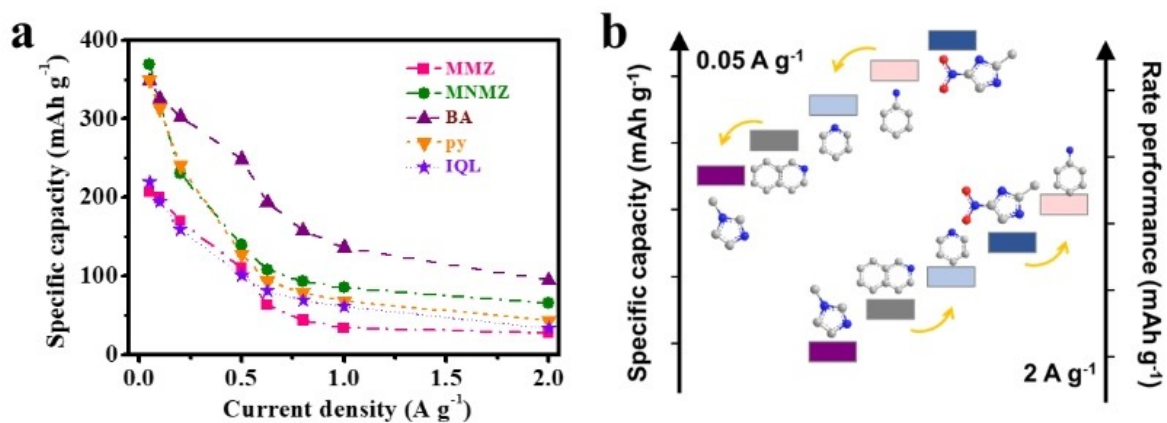
Figure S26. (a) Rate capability of MMZ, MNMZ, BA, py and IQL in a half cell. (b) Comparison of reversible capacity and rate performance of hard carbon materials obtained from different reactive small molecules.

Table S1. The surface areas and total pore volume of hard carbon materials from polymer.

Sample	Surface areas ($m^2 \ g^{-1}$)	Total pore volume ($cm^3 \ g^{-1}$)
MMZ	0.404	0.00940
MNMZ	68.1	0.408
py	5.27	0.0596
BA	5.51	0.00264
IQL	0.739	0.000970

Table S2. XRD fitting data of hard carbon materials from polymer.

Sample	Peak type	Peak position (degree)	FWHM
MMZ	002	24.00	7.14
	100	44.11	6.90
BA	002	23.54	7.54
	100	44.30	6.83
MNMZ	002	23.46	8.52
	100	44.39	6.34
IQL	002	24.54	5.95
	100	43.81	5.42
py	002	24.20	6.26
	100	43.99	5.77

Table S3. Raman fitting data of hard carbon materials from polymer.

Sample	Peak type	Area Fit	Max Height	A_G/A_D	I_G/I_D	La (nm) (A_G/A_D)	La (nm) (I_G/I_D)
MMZ	D	213146.6	1362.0	0.92	1.43	17.69	27.49
	G	196368.9	1949.9				
MNMZ	D	254522.2	1699.3	0.89	1.42	17.18	27.23
	G	227776.3	2409.7				
py	D	363264.8	2122.9	0.79	1.32	15.24	25.27
	G	288394.6	2794.0				
BA	D	780748.3	3529.8	0.51	0.95	9.74	18.24
	G	395955.4	3354.1				
IQL	D	278086.6	1680.9	0.72	1.17	13.78	22.38
	G	199604.1	1959.7				

NOTE:

It seems that the fitted Raman results have a significant distinction from that of XRD and we have analyzed the reasons for this result. Since the Raman activation pattern corresponds to in-plane vibration, the relationship between Raman (e.g. I_D/I_G) and the microcrystalline size L_a, which reflects the defect density or microcrystalline boundary along the base surface of the graphite material, is investigated. Tuinstra and Koenig[21] proposed a linear relationship between I_G/I_D and L_a from log-log plots of these two parameters, while L_a is determined by XRD measurements. Knight and White[22] added some of the data collected in the literature to Tuinstra and Koening's results and came up with the L_a=4.4/(I_D/I_G) (nm) equation, but the data was clearly scattered. Cancado et al.[23] measured Raman spectra in the range of 1.92 eV (647 nm) to 2.71 eV (457.9 nm) using different excitation laser energies (wavelengths) for DLC films that were heat treated at different temperatures between 1800 and 2700 °C. They also measured the XRD profiles of 100 diffraction lines using synchrotron radiation and determined the L_a values based on Scherrer's equation for the form factor K=1.84, after

correcting for the inherent instrument broadening and referring to the profile of a standard Si sample. They obtained a linear relationship between A_G/A_D and L_a plots for each excitation energy and came up with an equation,

$$L_a \text{ (nm)} = 560/E^4 * A_G/A_D = (2.4 \times 10^{-10}) \lambda_{nm}^4 (A_G/A_D)$$

Where E is the laser energy in eV and λ is the laser wavelength in nm. When λ=514.5 nm, the same as that used by Knight and White equations (1) becomes L_a=16.5/ (A_D/A_G), although considering a slight difference between A_D/A_G at 1600 and 2900 °C, But the coefficient of 16.5 is much larger than the 4.4 reported by Knight and White, Maslova et al.[24] measured Raman spectra at various excitation laser energies of 1.58-2.71eV, and used Kα(Cu) to measure the 110 diffraction pattern to determine the L_a value of K=1.84. For different coke types and different HTTS, the relationship between I_D/I_G and E^4 is different, and the relationship obtained at the excitation energy of 2.41 eV is L_a=12.26/(I_D/I_G) (nm) (wavelength 514.5 nm).

Nikiel and Jagodzinski[25] also reported differences from the equations proposed by Knight and White on the A_G/A_D and L_a nuclear graphite diagrams. Cuesta et al.[26] found that for various carbon materials, I_D/I_G and L_a curves are significantly dispersed. As mentioned above, to assess the intensity ratio of peak D to peak G, some authors use I_D/I_G, while others use A_D/A_G, although in some cases the D-peak is obtained as a double peak. In some literature, in order to obtain a good D-peak, the spectrum is divided into several peaks, up to five, and A_D is obtained, thus significantly modifying A_G/A_D. However, some researchers evaluate L_a based on a 100 diffraction pattern of K=1.84 and K=0.94, other authors use the average distance between defects determined from STM images instead of L_a.

Although various experimental and theoretical discussions of Raman spectroscopy have reported the fabrication of carbon materials, the relationship of A_D/A_G and I_D/I_G to structural parameters such as L_a has not been determined. Based on the current experimental results, the

relationship graphs between A_D/A_G and I_D/I_G and L_a are full of ambiguations, so it is difficult to be used as a general parameter to characterize the structure of carbon materials.

Table S4. A Breakdown of the Capacity Obtained on Each of the Three Micro-structures (Amorphous, Dispersion region, Graphite layer/Pore) for the Five Different Hard Carbon at a Rate of 50 mA g^{-1} between 2.8 and 0.01 V[a]

Carbon	d (nm)	L_a (nm)	Number of layers	Total capacity (mAh g^{-1})	Slope capacity (mAh g^{-1}) (%)	Dispersion capacity (mAh g^{-1}) (%)	Plateau capacity (mAh g^{-1}) (%)
BA	0.372	4.31	5.38	347.6	183.4 (52.8)	109.9 (31.6)	54.3 (15.6)
MNMZ	0.377	3.22	4.07	369.2	142.5 (38.6)	83.9 (22.7)	149.8 (40.6)
py	0.358	5.42	3.19	349.2	161.4 (46.2)	131.1 (37.5)	55.7 (16.0)
MMZ	0.364	2.85	2.90	206.5	96.6 (46.8)	51.1 (24.7)	58.8 (28.5)
IQL	0.365	3.00	2.13	220	120.8 (54.9)	69.8 (31.7)	29.4 (13.4)

[a]Electrochemical profiles are shown in Figures 4a−4b and S9.

Table S5. Contributions of adsorption capacity, disperse layer capacity, filling capacity of embedded pores and their cross-sectional areas of samples prepared with different spatial precursors.

Samples	Cross-sectional area$_L$ (nm^2)	Cross-sectional area$_G$ (nm^2)
MNMZ	2.43	7.46
MMZ	2.07	3.95
BA	3.21	14.07
py	3.88	8.50
IQL	2.19	2.47

Note: Cross-sectional area$_L$ (S_L)=2*d*L_a;

Cross-sectional area$_G$ (S_G)= 2*d*L_a*(n-1);

Table S6. Contribution ratio of capacitive-controlled charge storage from 0.2 to 2 mV s^{-1}.

Sample	Scan rate (mV s^{-1})			
	0.2	0.5	1	2
py	55.7	60.1%	62.5%	83.4
MNMZ	72.3	81.7%	89.5%	94.8
IQL	68.6	79.1%	85.3%	81.6
MMZ	53.4	63.9%	74.3%	82.8
BA	62.4	67.5%	90.4%	95.9

Table S7. Content of each element base on XPS.

Sample	N content (at%)	O content (at%)	Total content (at%)
MMZ	1.67	6. 8	8.47
MNMZ	3.71	6.42	10.13
py	2.04	6.85	8.89
BA	0.37	7.99	8.36
IQL	2.58	6.01	8.59

Reference:

1. G. Chen, X. Zhou, Y. Bai, Y. Yuan, Y. Li, M. Chen, L. Ma, G. Tan, J. Hu, Z. Wang, F. Wu, C. Wu, J. Lu, *Nano Energy* 2019, *56*, 884−892.

2. F. Wu, L. Liu, Y. Yuan, Y. Li, Y. Bai, T. Li, J. Lu, C. Wu, *ACS Appl. Mater. Interfaces* 2018, *10* **(32)**, 27030−27038.

3. Y. Li, Y. Yuan, Y. Bai, Y. Liu, Z. Wang, L. Li, F. Wu, K. Amine, C. Wu, J. Lu, *Adv. Energy Mater.* 2018, *8* **(18)**, 1702781.

4. G. Porod, *Kolloid-Zeitschrift* 1951, *124* **(2)**, 83−114.

5. G. Kresse, Furthmüller, *J. Comput. Mater. Sci.* 1996, **6**, 15−50.

6. G. Kresse, Furthmüller, *J. Phys. Rev. B* 1996, **54**, 11169−11186.

7. J. P. Perdew, K. Burke, M. Ernzerhof, *Phys. Rev. Lett.* 1996, **77**, 3865−3868.

8. G. Kresse, D. Joubert, *Phys. Rev. B* 1999, **59**, 1758−1775.

9. P. E. Blöchl, *Phys. Rev. B* 1994, **50**, 17953−17979.

10. S. Grimme, J. Antony, S. Ehrlich, S. Krieg, *J. Chem. Phys.* 2010, **132**, 154104.

11. S. Grimme, S. Ehrlich, L. Goerigk, *J. Comp. Chem.* 2011, **32**, 1456−1465.

12. F. Legrain, J. Sottmann, K. Kotsis, S. Gorantla, S. Sartori, S. Manzhos, *J. Phys. Chem. C* 2015, **119**, 13496−13501.

13. F. Legrain, K. Kotsis, S. Manzhos, *MRS Adv.* 2016, **1**, 3069−3074.

14. L. Zhong, J. Li, Y. Li, H. Lu, H. Du, L. Gan, C. Xu, S. W. Chiang, F. Kang, *J. Phys. Chem. C* 2016, **120**, 23239−23245.

15. O. I. Malyi, K. Sopiha, V. V. Kulish, T. L. Tan, S. Manzhos, C. Persson, *Appl. Surf. Sci.* 2015, **333**, 235.

16. H. Jin, X. Feng, J. Li, W. Li, Y. Xia, Y. Yuan, C. Yang, B. Dai, Z. Lin, J. Wang, J. Lu, Wang, S. *Angew. Chem. Int. Ed.* 2019, **58** (*8*), 2379−2401.

17. L. G. Cancado, K. Takai, T. Enoki, M. Endo, Y. A. Kim, H. Mizusaki, A. Jorio, L. N. Coelho, R. Magalhes-Paniago, M. A. Pimenta, *Appl. Phys. Lett.* 2006, **88**, 163106.

18. Y. Qi, Y. Lu, F. Ding, Q. Zhang, H. Li, X. Huang, L. Chen, and Y. Hu, *Angew. Chem. Int. Ed.* 2019, **58**, 4361.

19. Z. Pei, Q. Meng, L. Wei, J. Fan, Y. Chen and C. Zhi, *Energy Storage Mater.* 2020, **28**, 55-63.

20. X. Feng, Y. Bai, L. Zheng, M. Liu, Y. Li, R. Zhao, Y. Li, C. Wu, *ACS Appl. Mater. Interfaces* 2021**, 13** (47), 56285−56295.

21. F. Tuinstra and J. L. Koenig, *J. Chem. Phys.* 1970, **53**, 1126-1130.

22. D. S. Knight, W. B. White *J. Mater. Res.* 1989, **4**, 385-393.

23. M. A. Pimenta, G. Dresselhaus, M. S. Dresselhaus, L. G. Cançado, A. Jorioa, and R. Saito, *Phys. Chem. Chem. Phys.* 2007, **9**, 1276-1290.

24. O. A. Maslova, M. R. Ammar, G. Guimbretière, J. N. Rouzaud, and P. Simon, *Phys. Rev. B* 2012, **86**, 134205.

25. L. Nikiel, P. W. Jagodzinski, *Carbon* 1993, **31(8)**: 1313-1317.

26. A. Cuesta, P. Dhamelincourt, J. Laureyns, *Carbon* 1994, **32(8)**: 1523-1532.